Defense Threat Reduction Agency
8725 John J. Kingman Road, MS-6201
Fort Belvoir, VA 22060-6201

DTRA-TR-18-71

TECHNICAL REPORT

Verification and Validation Report for the Radiation Protection Factor Methodology using Monte-Carlo n-Particle Code, version 6

October 2018

Prepared by:

MAJ Andrew W. Decker
Research and Development Directorate, Nuclear Science and Engineering Research Center (NSERC)

For:

U.S. Army Nuclear and Countering-WMD Agency (USANCA)

REPORT DOCUMENTATION PAGE

Form Approved
OMB No. 0704-0188

1. REPORT DATE *(DD-MM-YYYY)*	2. REPORT TYPE	3. DATES COVERED *(From - To)*
00-10-2018	Technical	01 JUN14 – 28 JUN18

4. TITLE AND SUBTITLE
Verification and Validation Report for the Radiation Protection Factor Methodology using Monte-Carlo n-Particle Code, version 6

5a. CONTRACT NUMBER
N/A

5b. GRANT NUMBER

5c. PROGRAM ELEMENT NUMBER

6. AUTHOR(S)
MAJ Andrew W. Decker, DTRA-NSERC

5d. PROJECT NUMBER

5e. TASK NUMBER

5f. WORK UNIT NUMBER

7. PERFORMING ORGANIZATION NAME(S) AND ADDRESS(ES)
Nuclear Science and Engineering Research Center (NSERC)
Suite 100, Bartlett Hall (Bldg. 753)
West Point, NY 10996

8. PERFORMING ORGANIZATION REPORT NUMBER

9. SPONSORING/MONITORING AGENCY NAME(S) AND ADDRESS(ES)
Mr. Mark Sward
Chief, Nuclear Effects Division (RD-NTE)
8725 John J. Kingman Road
Ft. Belvoir, VA 22060

10. SPONSOR/MONITOR'S ACRONYM(S)
DTRA/RD-NTE

11. SPONSORING/MONITORING AGENCY REPORT NUMBER
DTRA-TR-18-71

12. DISTRIBUTION AVAILABILITY STATEMENT
Distribution Statement A. Approved for public release; distribution is unlimited.

13. SUPPLEMENTARY NOTES

14. ABSTRACT
This report establishes the foundation for current and future Radiation Protection Factor (RPF) research using Monte-Carlo n-Particle Code v6 (MCNP6) within the Department of Defense (DoD). Specifically, this document provides the background, justification, and conclusions supporting the RPF-determination methodology established and employed by the Defense Threat Reduction Agency (DTRA).

15. SUBJECT TERMS
Radiation Protection Factor (RPF), Neutron Protection Factor (NPF), Gamma Protection Factor (GPF), Shielding, Neutron Spectroscopy, Bonner Spheres, MCNP, MAXED

16. SECURITY CLASSIFICATION OF:			17. LIMITATION OF ABSTRACT	18. NUMBER OF PAGES	19a. NAME OF RESPONSIBLE PERSON
a. REPORT	b. ABSTRACT	c. THIS PAGE			MAJ David Matters
Unclassified	Unclassified	Unclassified	SAR	75	19b. TELEPONE NUMBER (*Include area code*) (571) 616-5217

UNIT CONVERSION TABLE

U.S. customary units to and from international units of measurement*

U.S. Customary Units	Multiply by → / ← Divide by†		International Units
Length/Area/Volume			
inch (in)	2.54	$\times 10^{-2}$	meter (m)
foot (ft)	3.048	$\times 10^{-1}$	meter (m)
yard (yd)	9.144	$\times 10^{-1}$	meter (m)
mile (mi, international)	1.609 344	$\times 10^{3}$	meter (m)
mile (nmi, nautical, U.S.)	1.852	$\times 10^{3}$	meter (m)
barn (b)	1	$\times 10^{-28}$	square meter (m^2)
gallon (gal, U.S. liquid)	3.785 412	$\times 10^{-3}$	cubic meter (m^3)
cubic foot (ft^3)	2.831 685	$\times 10^{-2}$	cubic meter (m^3)
Mass/Density			
pound (lb)	4.535 924	$\times 10^{-1}$	kilogram (kg)
unified atomic mass unit (amu)	1.660 539	$\times 10^{-27}$	kilogram (kg)
pound-mass per cubic foot (lb ft^{-3})	1.601 846	$\times 10^{1}$	kilogram per cubic meter (kg m^{-3})
pound-force (lbf avoirdupois)	4.448 222		newton (N)
Energy/Work/Power			
electron volt (eV)	1.602 177	$\times 10^{-19}$	joule (J)
erg	1	$\times 10^{-7}$	joule (J)
kiloton (kt) (TNT equivalent)	4.184	$\times 10^{12}$	joule (J)
British thermal unit (Btu) (thermochemical)	1.054 350	$\times 10^{3}$	joule (J)
foot-pound-force (ft lbf)	1.355 818		joule (J)
calorie (cal) (thermochemical)	4.184		joule (J)
Pressure			
atmosphere (atm)	1.013 250	$\times 10^{5}$	pascal (Pa)
pound force per square inch (psi)	6.984 757	$\times 10^{3}$	pascal (Pa)
Temperature			
degree Fahrenheit (°F)	[T(°F) − 32]/1.8		degree Celsius (°C)
degree Fahrenheit (°F)	[T(°F) + 459.67]/1.8		kelvin (K)
Radiation			
curie (Ci) [activity of radionuclides]	3.7	$\times 10^{10}$	per second (s^{-1}) [becquerel (Bq)]
roentgen (R) [air exposure]	2.579 760	$\times 10^{-4}$	coulomb per kilogram (C kg^{-1})
rad [absorbed dose]	1	$\times 10^{-2}$	joule per kilogram (J kg^{-1}) [gray (Gy)]
rem [equivalent and effective dose]	1	$\times 10^{-2}$	joule per kilogram (J kg^{-1}) [sievert (Sv)]

*Specific details regarding the implementation of SI units may be viewed at http://www.bipm.org/en/si/.

†Multiply the U.S. customary unit by the factor to get the international unit. Divide the international unit by the factor to get the U.S. customary unit.

This page intentionally left blank.

Record of Changes

Version	Date	Changes

Table of Contents

1. V&V REPORT EXECUTIVE SUMMARY

Although the protection afforded by US Army vehicles against conventional weapons and improvised explosive devices has improved significantly in recent years, the degree of protection afforded against prompt and residual radiation originating from a nuclear weapon or improvised nuclear device is largely incorrect or unknown for a majority of military vehicles. In an apparent effort to reduce costs, requirements to provide Radiation Protection Factor (RPF) information for current vehicles were removed from most capability design documents following the end of the Cold War.

This report establishes the foundation for current and future RPF research using Monte-Carlo n-Particle Code v6 (MCNP6) [1] within the Department of Defense (DoD). Specifically, this document provides the background, justification, and conclusions supporting the RPF-determination methodology established and employed by the Defense Threat Reduction Agency (DTRA).

A RPF is calculated from the ratio of radiation dose outside (unshielded) compared to the dose present inside the vehicle (shielded) and may be determined using the equation

$$RPF = \frac{\text{Unshielded Dose (neutron + gamma)}}{\text{Shielded Dose (neutron + gamma)}}. \qquad (1)$$

Since neutrons and gamma rays represent the two most biologically significant sources of radiation following a nuclear detonation, a more detailed analysis of vehicle RPF can be obtained by defining both the neutron protection factor (NPF) and the gamma protection factor (GPF):

$$NPF = \frac{\text{Unshielded Neutron Dose}}{\text{Shielded Neutron Dose}}, \qquad (2)$$

$$GPF = \frac{\text{Unshielded Gamma Dose}}{\text{Shielded Gamma Dose}}. \qquad (3)$$

Consequently, a RPF value is an additive combination of GPF and NPF components, as shown in Equation 1. Of note, since neutron environments often result in secondary gamma rays due to neutron activation, a NPF_g can also be used to account for that dose contribution. The implication to be drawn from these three equations is the larger the RPF value, the better the degree of protection afforded by the vehicle or shelter. Additionally, due to the energy-dependent nature of these ratios, vehicle RPF values may fluctuate significantly between prompt and residual radiation environments, typically requiring separate assessments for each scenario.

The modeling and simulation (M&S) tool selected for the DTRA RPF methodology was the MCNP code. MCNP is an export-controlled radiation transport code developed and maintained by Los Alamos National Laboratory (LANL). It was selected by DTRA for incorporation into the RPF methodology due to its wide acceptance as the world's premier radiation transport code, as well as its proven record of successful independent verification and validation (V&V) [1].

Prior to computing protection factor estimates for US Army vehicles, the latest version of the code, MCNP6, had to undergo extensive V&V as a component of the DTRA RPF methodology. These V&V efforts incorporated numerous experiments utilizing a variety of simplified surrogate military vehicles and were based on established methodologies detailed in Cold War-era code validation reports [2-7]. Acceptability was achieved whenever the MCNP6-derived protection factors agreed within 10% of the experimentally-determined results, including associated uncertainty. Based upon this criteria, all V&V RPF evaluations using MCNP6 were successful.

The V&V process for this RPF methodology, which compares computational and experimental results, began in 2014 with a successful evaluation of the NPF for a steel cube exposed to a mono-energetic neutron source. Subsequent evaluations expanded to include GPF determinations and increased source term and vehicle surrogate complexities in a formal, deliberate plan to assess MCNP6 accuracy across a wide range of model and experiment intricacy. Recent evaluations have successfully determined the combined RPF for a vehicle surrogate with complex armor characteristics using a single poly-energetic source. This experimental and computational evaluation constituted the upper limit for laboratory-based V&V of the DTRA RPF methodology. Consequently, the next logical stage of test and evaluation (T&E) should include a full-sized US Army military vehicle.

In conclusion, based upon the numerous evaluations and successful findings detailed below, DTRA leadership fully endorses and approves the RPF methodology described herein.

2. PROBLEM STATEMENT

The US Army lacks the ability to accurately estimate the degree of radiological protection afforded to crews and passengers within modern combat and support vehicles. To address this requirement gap, DTRA and the US Army Nuclear and Countering Weapons of Mass Destruction Agency (USANCA) established the RPF methodology to quantify protection factor values for a variety of military vehicle surrogates. This RPF methodology, which utilizes MCNP6 to computationally estimate protection factors for surrogates, must first complete V&V before the methodology can be applied to a full-sized military vehicle evaluation.

Following a successful evaluation of the RPF methodology using a full-sized military vehicle, it will be possible to calculate accurate RPFs for a variety of US Army vehicles using MCNP6. When faced with a radiological environment, vehicle RPF values will inform decisions made at every military and DoD leadership level, from tactical vehicle orientation to strategic planning.

Due to the utility of RPF data, it is important to fully consider the risks associated with incorrectly determining RPF values alongside the benefits of correct assessments. Erroneously low RPF estimates could artificially constrain maneuver flexibility on a nuclear battlefield, thereby forcing commanders to assume unnecessary risk while maneuvering units. Conversely, falsely high RPF estimates could expose vehicle crews to unacceptable radiation levels and/or cause commanders to fail in reaching their military objectives. Only accurate and verifiable RPF values of military vehicles will correctly inform commanders and strategic decision-makers of optimal force employment and risk management on a nuclear battlefield.

2.1. M&S Intended Use

MCNP6 provides computational data to inform NPF, GPF, and RPF assessments for military vehicles or surrogates. These data are produced by MCNP6 as flux, pulse height, and/or energy deposition tallies for a given volume, both shielded and unshielded. Based on the current methodology, the M&S results are then converted to units of dose via flux-to-dose conversion factors or a dose equivalent calculation. This allows for both the additive assessment of neutron and gamma dose described above, as well as for a quantifiable comparison of the MCNP6-derived protection factor against experimentally-derived results. It is this comparison that is used to quantify the accuracy of the MCNP6 protection factor estimate, so MCNP6 represents an integral part of the RPF Methodology. Fig. 1 provides a graphic depiction of the RPF Methodology as a comparison of experimental to computational results, in this case for NPF calculations.

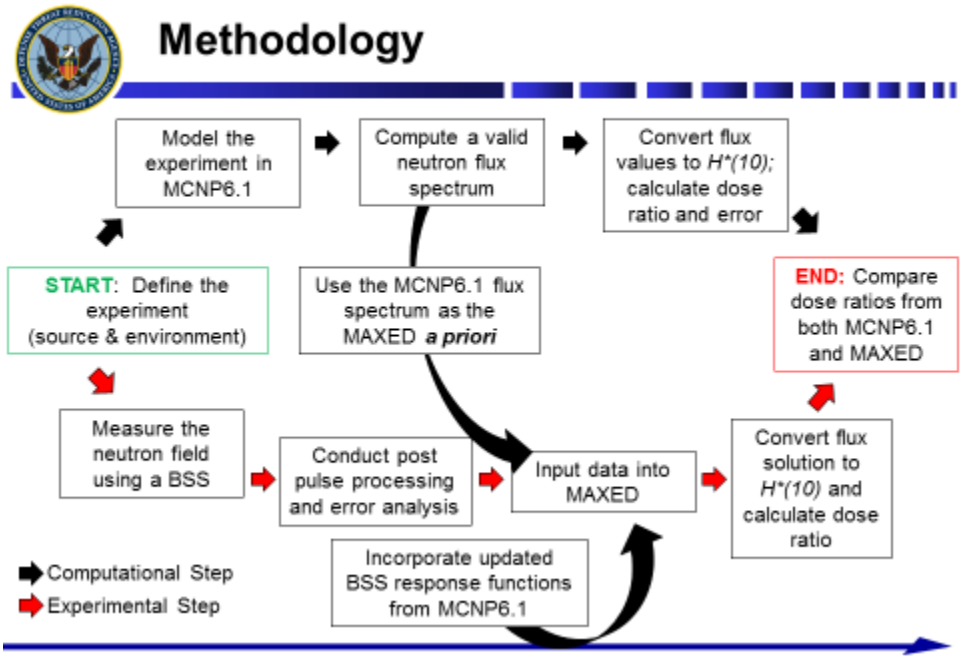

Figure 1. A graphic depicting the major experimental and computational steps involved in MCNP V&V for NPF estimates. Although individual steps differ, the same process is utilized to V&V MCNP6 for specific GPF and RPF estimates, as well.

2.2. M&S Overview

MCNP is the oldest and still most widely utilized radiation transport code in existence. First created at LANL in 1957, the code simulated neutral particle transport to enable predictions of radiation flux due to shielding and distance. It provides extremely accurate modeling for a variety of particle types, and previous versions of MCNP were repeatedly validated using both simple and complex geometries [8, 9]. Additionally, this code was originally validated against a benchmark test using a two-meter iron box and was trusted for RPF evaluations of numerous military vehicles, including the M60 and M1 Abrams main battle tank. More recently, MCNP6 was successfully used to calculate dose reduction factors for civilian vehicles following the Fukushima accident, which occurred in 2011 [10].

MCNP6 is the latest version of MCNP produced by LANL. The following discussion is intended only as an overview of the tremendous capabilities inherent within this computational tool. Information not provided within this report on the use of first principles by MCNP6 for modeling radiation transport is left to the explanations provided within the MCNP6 User's Manual. Additional V&V documentation can also be found at: https://laws.lanl.gov/vhosts/mcnp.lanl.gov /references.shtml#mc_verif.

MCNP6 includes the merger of MCNP5 and MCNPX and is capable of modeling three-dimensional geometries, the transport of 36 continuous-energy particle types, reactor fuel burn-up, and delayed-gamma emissions [1]. This latest version also boasts new tally, source, and variance reduction options, as well as an improved plotting capability [11]. Essentially, MCNP6 represents the most comprehensive update to the MCNP code in recent decades, a fact which makes this version, once sufficiently validated, attractive to the US Army for solving the problem of vehicle RPF assessment. Additionally, MCNP6 includes support for unstructured mesh (UM) geometries, which is essential for facilitating conversion of military vehicle Computer-Aided Design (CAD) models into MCNP input files[12].

Similar to previous versions of MCNP, MCNP6 operates from a user created input file, which contains all the necessary information to enable the program to model any given experiment. First among this information is the definition of the geometric spaces within the problem, known as cells, and how they exist within or among one another. Cells may be designed simplistically, such as a set of cubical boxes, or in as detailed a manner as a nuclear reactor, complete with fuel and control rods. Along with cell positioning, an assignment of material density is also possible.

MCNP6 input parameters also govern the material composition for all cells, allowing the user to define any medium by its atomic composition. These data affect neutron transport through calculations of mean free path and reaction rate densities, as discussed earlier. Additionally, the atomic structure of each material greatly alters the calculations of particle scattering angle, absorption, and energy deposition. The radiation source may also be defined therein, including its shape, location, radiation type, and emitted particle energies. This includes manipulation of initial particle direction and energy spectrum. Lastly, MCNP6 allows the user to tailor the results, incorporating directions for how and what specific data the code displays.

MCNP6 also offers a number of built-in variance reduction features. These represent established techniques and fall under the broad categories of population control, modified sampling methods, and partially deterministic methods [1]. For a complete definition of each technique, readers are encouraged to consult the MCNP6 User's Manual; however, each feature is designed to allow users to obtain more precise and computationally efficient results. Nevertheless, despite these hard-coded variance reduction techniques, other user-implemented forms of variance reduction may also be employed.

2.3. M&S Application

As detailed above, experiments measuring the NPF, GPF, and/or RPF for a given military vehicle or surrogate are also modeled in MCNP6. The MCNP6 input files include the geometric and material isotopic properties of the military vehicle or surrogate under evaluation, as well as a simulation of the radiation source term and its components.

For prompt and residual GPF estimates, the MCNP6 input file includes an energy deposition tally (F6) for all detector regions within the vehicle. This computation constitutes the "shielded" gamma assessment. The same tallies and locations are utilized with the vehicle and associated materials absent, which represent the "unshielded" assessment. Gamma radiation doses are then calculated for both the shielded and unshielded configurations, and a GPF ratio estimate is calculated from those values. This applies to both point and distributed sources of gamma radiation.

For prompt NPF (NPF) estimates, the MCNP6 input file includes a neutron flux tally (F4) for all detector regions within the vehicle, which constitutes the "shielded" neutron assessment. The same tallies and locations are utilized with the vehicle and associated materials absent, which represents the "unshielded" assessment. Neutron radiation doses are then calculated for both the shielded and unshielded configurations using flux-to-dose conversion factors published in 2005 [13], and a prompt NPF ratio estimate is calculated from those values.

For NPF calculations that include secondary gammas (NPF_g), a similar process to the prompt NPF determination will occur; however, an F6 tally will also be used within the detector regions to account for secondary photons. Additionally, the activation card (ACT) is employed for all constituent materials of the vehicle and the MCNP6 mode is set to tally both neutrons and gamma rays. Based upon the combined neutron and gamma dose estimates for the shielded and unshielded computations, a NPF_g will be determined.

Lastly, to derive simulated RPF values from MCNP6, the same procedure described above for NPF_g is applied whenever the vehicle and environment are exposed to a mixed neutron and gamma source. Of note, MCNP6 offers the ability to calculate deposited dose values based upon ICRP values for neutron and gamma energy deposition; however, organically-calculated doses and associated protection factors have not been thoroughly evaluated for inclusion within the RPF methodology at this time. All calculations of dose equivalence and flux-to-dose conversion took place outside the code to facilitate a more open and transparent review of the procedures and subsequent conclusions.

2.4. V&V Scope

The focus of this V&V report is limited to the RPF methodology as it applies to surrogate military vehicles, and MCNP6 accuracy and reliability is only one component of that process. As noted above, MCNP6 has undergone rigorous V&V by LANL and external partners; however, it was never specifically evaluated for computation of vehicle protection factors within neutron and gamma radiation environments. As such, this report focuses on the V&V of the RPF methodology, which includes MCNP6, while future full-vehicle T&E conducted by USANCA and other DTRA partners will provide the final accreditation of MCNP6 for RPF determination.

3. M&S REQUIREMENTS AND ACCEPTABILITY CRITERIA

This section describes the MCNP6 requirements tied directly to its intended use in generating accurate NPF, GPF, and RPF estimates for vehicle surrogates, as well as military vehicles. The derived acceptability criteria were determined by the RPF Research Team in 2014 and served as

the basis for the DTRA Experimental Test Plan (ETP) objectives during WSMR experimentation in 2015, 2016, and 2017. These should form the foundation for future MCNP6 requirements whenever it is used for RPF computation. The quantitative and qualitative metrics used to measure MCNP6 success were similarly defined and prioritized.

Of note, experimentally-measured neutron spectra were almost entirely unfolded from Bonner Sphere Spectrometer measurements using the Maximum Entropy Deconvolution (MAXED) code. The MAXED Few Channel software was authored specifically for the purposes of unfolding neutron spectra from Bonner Sphere data and uses the principle of maximum entropy in the deconvolution of multisphere spectroscopy data [14]. The maximum entropy principle suggests that, for problems where multiple probability distribution solutions exist, the best solution is the one with the largest degree of entropy, or uncertainty in a random variable. This provides MAXED a method of inference which is both consistent and unbiased [15].

Before spectrum deconvolution begins, however, some information must already exist about the neutron source. Whether derived by calculation, computation, or experimentation, a default spectrum, or a priori, is required to support the deconvolution calculation [15]. The MAXED program uses this default spectrum as a baseline for the generated answer, even if the provided spectrum is little more than conjecture. To accomplish this, the program evaluates a number of solutions which all match the measured response functions, and the solution most closely matching the default spectrum is selected. The code then provide the solution spectra in a quantity of neutron flux, which is typically converted to neutron lethargy flux, which is commonly used in nuclear reactor analysis to gauge the average logarithmic energy loss of elastically scattered neutrons, and described as

$$Lethargy\ Flux = \frac{\phi_g}{U_g} = \frac{\phi_g}{\ln\left[\frac{E_g}{E_{g-1}}\right]} \left[\frac{n}{cm^2 \Delta Us}\right], \qquad (4)$$

where the neutron flux, ϕ_g, divided by the neutron unit lethargy, U_g, provides lethargy flux in units of flux per unit lethargy.

Based upon these factors, the relationships among the requirements, acceptability criteria, and metrics/measures are provided below in Table 1.

Table 1: The detailed relationship between the MCNP6 requirements, acceptability criteria and metrics used to measure success or failure.

#	MCNP6 Requirement	Acceptability Criteria	Metrics/Measures
1	Compute neutron lethargy flux spectrum present in the free field and due to neutron irradiation.	1.1 Relative intensity agreement 1.2 Peak location agreement	Spectroscopic analysis and comparison against experimental results
2	Compute neutron lethargy flux spectrum present within a vehicle surrogate due to neutron irradiation.	2.1 Intensity agreement 2.2 Peak location agreement	Spectroscopic analysis and comparison against experimental results
2'	Compute secondary gamma-rays from neutron activation within a vehicle surrogate.	2.1' Relative intensity agreement 2.2' Peak location agreement	Spectroscopic analysis and comparison against experimental results
3	Provide an accurate NPF based on requirements 1 & 2	Accuracy found to be within 10% of the experimentally-determined value, including uncertainty	Calculated NPF values for an identical surrogate used in a similar physical experiment
3'	Provide an accurate NPF_g based on requirements 1, 2, & 2'	Accuracy found to be within 10% of the experimentally-determined value, including uncertainty	Calculated NPF_g values for an identical surrogate used in a similar physical experiment
4	Estimate deposited energy and spectrum present within a given volume or crystal exposed to gamma irradiation in a free field environment.	4.1 Relative intensity agreement 4.2 Peak location agreement	Spectroscopic analysis and comparison against experimental results
5	Estimate deposited energy and spectrum within a given volume or crystal exposed to gamma irradiation while inside a vehicle surrogate.	5.1 Relative intensity agreement 5.2 Peak location agreement	Spectroscopic analysis and comparison against experimental results
6	Provide an accurate GPF based on requirements 4 & 5	Accuracy found to be within 10% of the experimentally-determined value, including uncertainty	Calculated GPF values for an identical surrogate used in a similar physical experiment
7	Simulate neutron and gamma transport to facilitate an accurate estimation of vehicle surrogate RPF, based on requirements 3 and 6.	Accuracy found to be within 15% of the experimentally-determined value, including uncertainty	Calculated RPF values for an identical surrogate used in a similar physical experiment

4. M&S ASSUMPTIONS, CAPABILITIES, LIMITATIONS, & RISKS/IMPACTS

This section typically describes known factors that constrain the development and/or use of the M&S tool or that impede the V&V effort. Due to the widespread use of MCNP6 and its thorough

VV&A by LANL and others, the majority of these sections will simply reference the MCNP6 User's Manual. However, a few important caveats are worth mentioning as MCNP6 is further researched and applied to the estimation of protection factors for military vehicles, which are addressed in the following sections below.

4.1. M&S Capabilities

For a complete list and descriptions of MCNP6 Capabilities, please refer to the User's Manual [1].

4.2. M&S Limitations

The primary limitations of MCNP6 center around the accuracy of the model in representing both a vehicle surrogate and the source term. In regards to a vehicle surrogate, and by extension a full vehicle model, both the geometry and isotopic information about the shielding material are vitally important to achieving an accurate assessment from MCNP6. Although prior research suggests that geometry is more significant [16], the isotopic mixtures used in the vehicle armor and framing will heavily influence the scatter and absorption of both neutrons and gammas, and the production of secondary gammas by neutron-induced reactions, which affects calculated dose values.

Additionally, any MCNP6 simulated source term must also accurately reflect any testing and/or likely hostile environments to the greatest extent possible. RPF predictions for any surrogate or vehicle based on a given source term may prove unreliable if the same system is exposed to different incident radiation spectra. Such a change in RPF values is believed to be especially prominent in mixed neutron and gamma environments; however, the degree of such a difference is not yet quantified and would largely depend on the differences in incident radiation environments. For now, the most that can be done to minimize those differences is to establish two likely scenarios for evaluation, which are prompt and residual radiation environments.

4.3. M&S Risks/Impacts

Due to the utility of RPF data, it is important to fully consider the risks associated with incorrectly determining RPF values alongside the benefits of correct assessments. Erroneously low RPF estimates could artificially constrain maneuver flexibility on a nuclear battlefield, thereby forcing commanders to assume unnecessary risk while maneuvering units. Conversely, falsely high RPF estimates could expose vehicle crews to unacceptable radiation levels and/or cause commanders to fail in reaching their military objectives. Only accurate and verifiable RPF values of military vehicles will correctly inform commanders and strategic decision-makers of optimal force employment and risk management on a nuclear battlefield.

Likewise, the risk of delaying the final accreditation of MCNP6 by USANCA for RPF assessments of current military vehicles is also a consideration. For this very reason, future DTRA evaluations of MCNP6 were curtailed to expedite the final T&E needed to certify MCNP6 for RPF assessments by USANCA. Consequently, in the interests of expediently supporting the warfighter, a number of planned evaluations are now considered unnecessary, and these can be seen below in Figs. 2 and 3.

5. V&V TASK ANALYSIS

DTRA RPF research first began in 2013 at the Air Force Institute of Technology (AFIT) with an exploratory comparison of MCNP6 NPF estimates against those measured experimentally using a steel vehicle surrogate and a mono-energetic neutron source. Completed in 2014, the NPF results differed by less than 1% [17], which strongly supported further RPF-related evaluations of MCNP6 estimates.

Based upon this initial success, a program manager (PM) was appointed from DTRA's Nuclear Science and Engineering Research Center (NSERC), which is located at the United States Military Academy (USMA) at West Point, NY. An RPF research campaign plan was drafted and approved, which utilized a series of increasingly complex experimental designs to compare against equivalent MCNP6 estimates. Specifically, the Experimentation Schedule varied both the materials and geometry between either simple (S) or complex (C), as well as the source energy spectra as either mono- (M) or poly- (P) energetic, as shown below in Fig. 2. This established a logical, sequential V&V process for MCNP6-derived RPF estimates for DTRA. Due to successful validations of MCNP6 protection factor estimates to date, the DTRA-led experimental portion of this research plan is now considered complete, with the exception of the actual military vehicle test and final V&V of MCNP6 to be completed by USANCA.

Additionally, the RPF campaign plan and experimental schedule relied heavily upon research integration across the DoD degree-granting institutions, which provided the benefit of low-cost research and student involvement with the drawback of slower research progression due to the academic year (AY) schedule. Along with USMA and AFIT, the United States Naval Academy (USNA) and Naval Postgraduate School (NPS) were identified early on as potential contributors to RPF research. The degree of integration, as well as the current progress of RPF research, is illustrated in both Figs. 2 and 3, shown below.

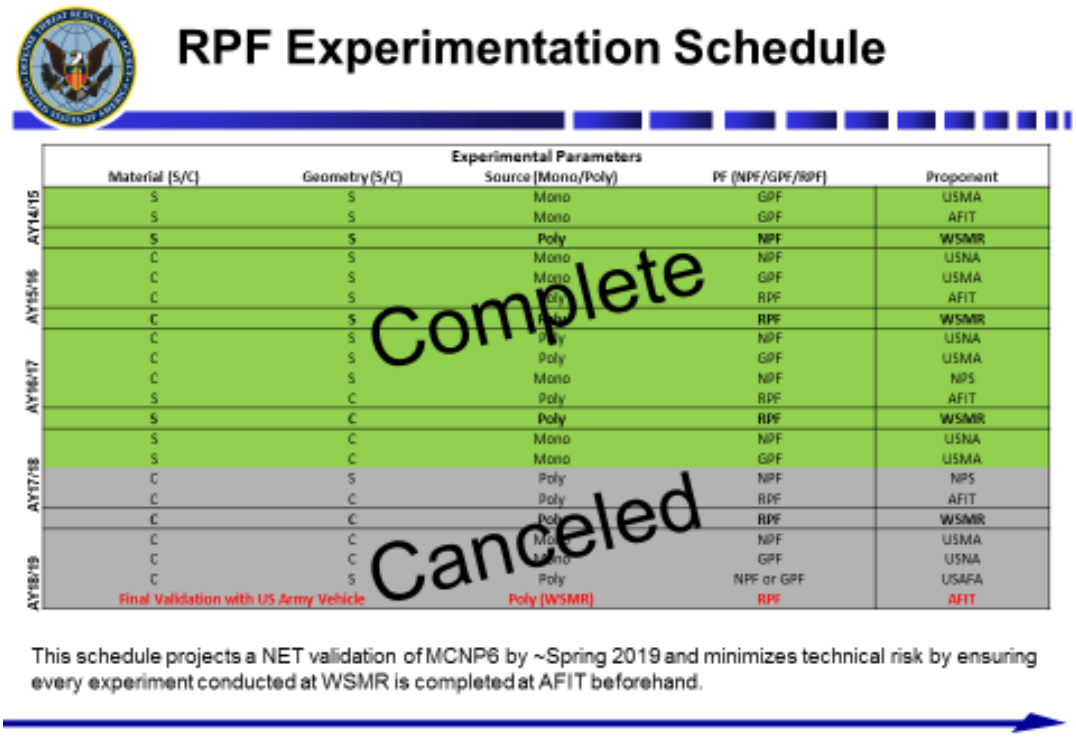

Figure 2. A schedule of RPF experiment parameters used to coordinate and synchronize the research efforts of DoD degree-granting institutions to collectively V&V MCNP6 for RPF estimates of military vehicles.

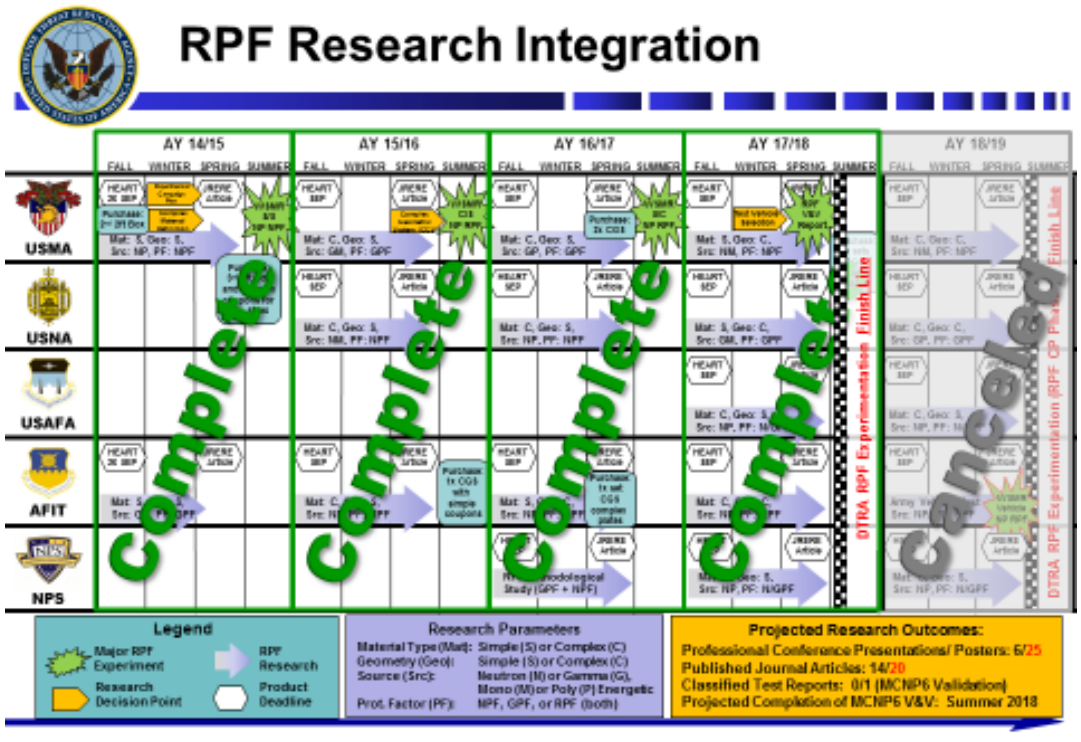

Figure 3. A diagram of RPF Research integration across the DoD degree-granting institutions, as well as anticipated outcomes. RPF experimentation was expected to complete in Spring of 2019; however, this was adjusted in 2017 to a completion date of June 2018.

In AY 14/15, RPF research integration produced a successful V&V of MCNP6-derived GPF estimates at AFIT [16], as well as an initial RPF research project at USMA. Most notably, AY 14/15 culminated in a NPF experiment conducted at the White Sands Missile Range (WSMR) Fast Burst Reactor (FBR), which yielded relevant results due to its combined watt-fission neutron and gamma source spectra [18]. This experiment also marked the initial support of RPF research by students and faculty from USNA, as described below in Fig. 4. All experimentation conducted in AY 14/15, including the experimentation at WSMR, utilized the same steel vehicle surrogate used previously at AFIT.

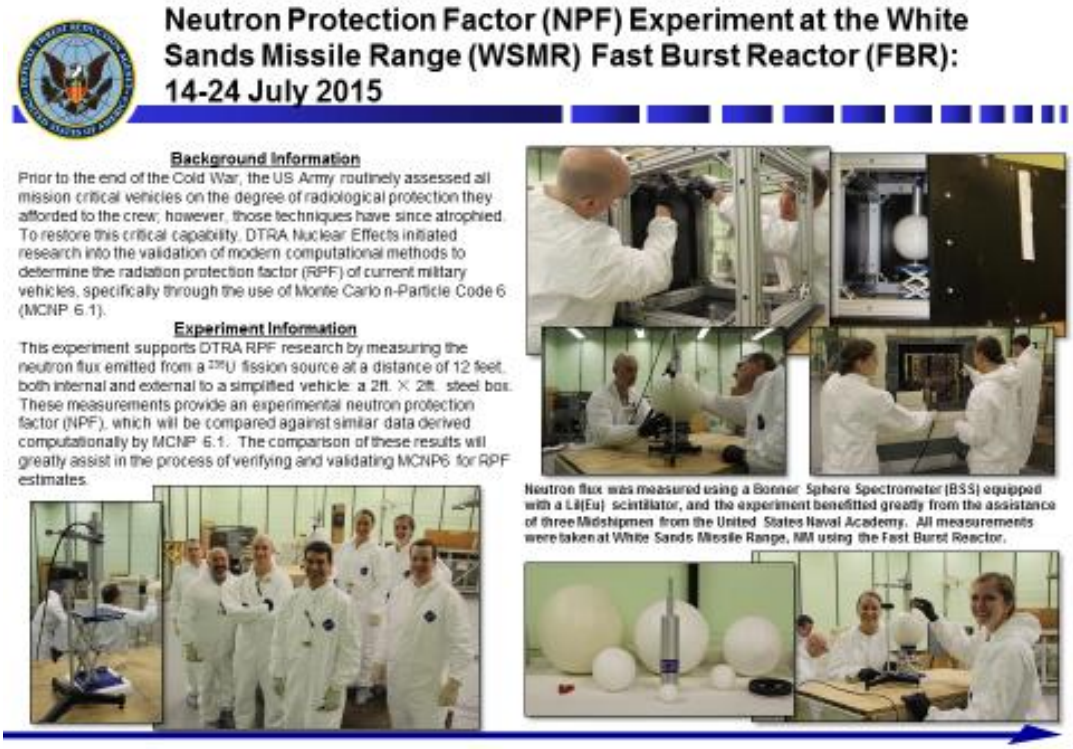

Figure 4. A storyboard describing the 2015 Joint NPF research conducted by DTRA at the WSMR FBR, which incorporated students and researchers from DTRA, USMA, USNA, and AFIT.

RPF research to support the V&V of MCNP6 during AY15/16 maintained the original simplified vehicle geometry; however, the material layers were made more complex with the combination of steel, a glass-reinforced plastic (FR-4), and aluminum. Together, these material layers represented a vehicle frame, anti-spallation liner, and vehicle skin, respectively. The new armored materials and layered configuration also provided MCNP6 with a more challenging radiation transport problem. Despite this, MCNP6 proved successful in estimating NPF values for the vehicle surrogate exposed to mono-energetic 14.1 MeV neutrons at USNA [19]. Additionally, two GPF studies conducted at USMA with ^{137}Cs gamma-ray sources provided acceptable experimental and computational results (<10% disparity), and one even incorporated the head of an anthropomorphic phantom into both the experiment and modeling [20, 21]. AY 15/16 then concluded with another

successful experiment conducted at the WSMR FBR, this time also evaluating MCNP6 estimations using the complex materials and simplified geometry described above [22], as shown below in Fig. 5.

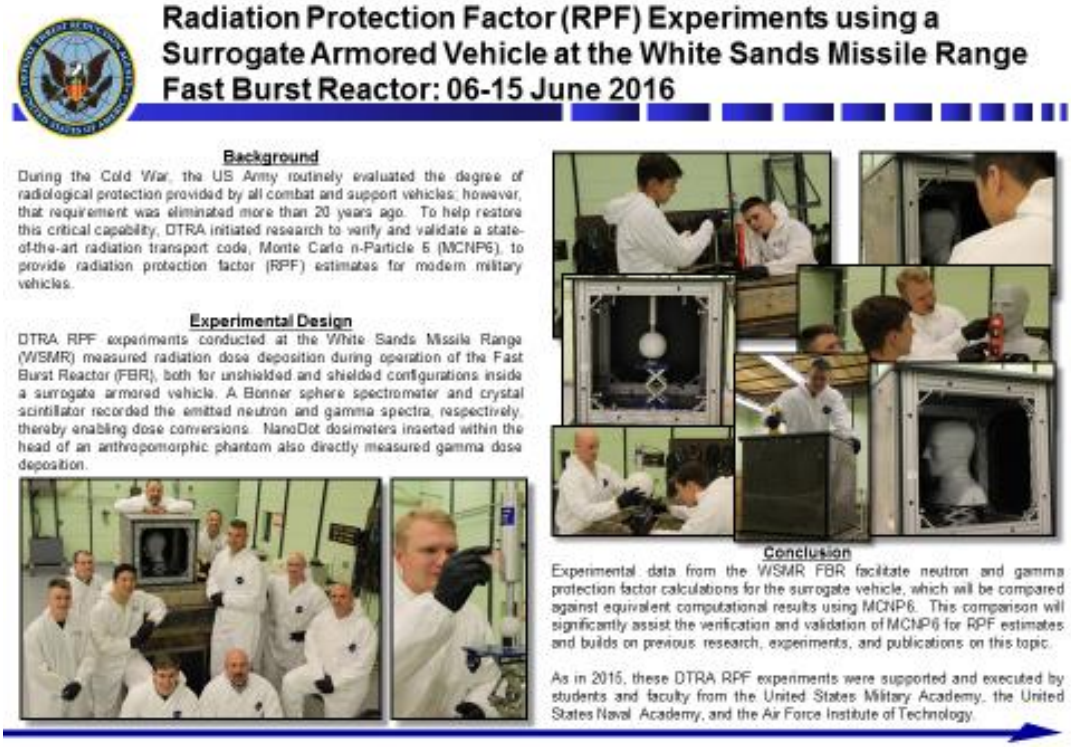

Figure 5. A storyboard describing the 2016 Joint NPF research conducted by DTRA at the WSMR FBR, which incorporated students and researchers from DTRA, USMA, USNA, and AFIT

RPF research conducted in AY16/17 maintained both the complex materials and simplified geometry used in the previous experimental design; however, these experiments incorporated poly-energetic source terms to increase M&S complexity. As before, USNA conducted a NPF study using MCNP6, and USMA evaluated MCNP6 GPF estimates of the armored surrogate using a ^{60}Co gamma-ray source. Once again, the MCNP6 estimates proved accurate within 10% for both studies. Additionally, AY16/17 marked the start of Naval Postgraduate School (NPS) support to the RPF research effort. This began with an experiment conducted at the Lawrence Livermore National Laboratory (LLNL), which evaluated MCNP6 NPF estimates of the armored surrogate using an extremely well-characterized ^{252}Cf neutron source for the experimental measurements. Results from this study further supported MCNP6 accuracy for RPF determinations. Lastly, a final experiment was conducted at the WSMR FBR, which evaluated the NPF of a new vehicle surrogate. This new surrogate provided a more complex geometry, one consisting of two nested cubes, while each was composed of simple materials, in this case rolled homogenous steel. The results of this first experiment into the RPF of a complex surrogate proved successful [23], and this type of surrogate formed the basis for experimentation and MCNP6 evaluation throughout the following AY.

During AY17/18, experiments conducted at both USNA and USMA evaluated the NPF and GPF of the complex geometric surrogate, respectively. While still unpublished, these results further

support the theoretical and demonstrated accuracy of MCNP6 to adjudicate difficult radiation transport problems and, subsequently, support accurate protection factor assessments.

In summary, prior experimental and computational evaluations of MCNP6 and its ability to accurately predict protection factors for vehicle surrogates using the RPF Methodology proved extremely successful [16-23]. Future USANCA V&V efforts will simulate residual GPF values for a full-size military vehicle based on prior experimentation and should include a full-vehicle outdoor test to conclusively quantify MCNP6 estimates of prompt RPF values. As mentioned previously, the formal V&V of MCNP6 to provide reliable RPF estimates for US Army vehicles will ultimately culminate in a full Army vehicle experiment, which will be conducted by USANCA and other partners.

5.1. Data V&V Tasks Analysis

5.1.1. Data Verification Tasks Analysis

Definition of Verification:

1. The process of determining that a model implementation and its associated data accurately represent the developer's conceptual description and specifications.

2. The process of determining that a model or simulation faithfully represents the developer's conceptual description and specifications. Verification evaluates the extent to which the model or simulation has been developed using sound and established software and system engineering techniques.

For the purposes of this document, "verification" is achieved through a series of evaluations on spectroscopic agreement between measured and MCNP6-estimated neutron and gamma spectra. Since calculations of absorbed dose are directly correlated to the type and energy distribution of incident radiation, a direct comparison of equivalent experimental and computational spectra is necessary to ensure MCNP6 correctly simulates the involved physics. The task matrix provided below in Table 2 compares these spectra, and thereby supports MCNP6 verification.

As described above in Fig. 2, studies varied both the materials and geometry between either simple (S) or complex (C), as well as the source energy spectra as either mono- (M) or poly- (P) energetic, as shown below in Tables 2 & 3. This established a logical, sequential V&V process for MCNP6-derived RPF estimates for DTRA.

Table 2: List of verification tasks for the RPF methodology. These focus on evaluating the level of agreement between measured and MCNP6-estimated neutron and gamma spectra using a deliberate and sequential combination of simple (S) and complex (C) materials and geometry, as well as source spectra.

Verification Tasks				
#	Material (S/C)	Geometry (S/C)	Source (Mono/Poly)	Spectra
1	S	S	Mono	Neutron
2	S	S	Mono	Gamma
3	**S**	**S**	**Poly**	**Neutron**
4	C	S	Mono	Neutron
5	C	S	Mono	Gamma

6	C	S	Poly	Gamma + Neutron
7	**C**	**S**	**Poly**	**Neutron**
8	C	S	Poly	Neutron
9	C	S	Poly	Gamma
10	**S**	**C**	**Poly**	**Neutron**
11	S	C	Poly	Gamma

To accomplish this task, spectroscopic data for both neurons and gamma rays were measured using a variety of devices. The principle radiation detector utilized to measure neutron spectra was the Bonner Sphere Spectrometer (BSS), which was paired in all cases with a 4×4 mm LiI(Eu) scintillator crystal. In the case of gamma ray spectra, a variety of sizes and types of scintillators were used, including $LaBr_3$ and NaI. The results of all experimental and computational spectral comparisons for both neutron and gamma rays are discussed in greater detail within the referenced articles.

The research findings for each individual task are included below, along with a listed citation for the conclusions presented.

5.1.1.1 Task 1

#	Material (S/C)	Geometry (S/C)	Source (Mono/Poly)	Spectra
1	S	S	Mono	Neutron

The following text, images, and data were published as:
A.W. Decker, M.P. Shannon, J.A. Clinton, J.W. McClory, S.R. McHale, "Verification and Validation of Monte Carlo N-particle Code 6 (MCNP6) with Neutron Protection Factor Measurements of an Iron Box", *Journal of Radiation Effects, Research and Engineering*, vol. 33, no. 1-E, pp. 252-259, May 2015.

Spectral Deconvolution of Poly-energetic Neutron Sources
Future investigations of military vehicles exposed to various neutron sources will likely require deconvolution of the measured and MCNP6-simulated spectrometer responses, since spectrometer output does not provide direct information regarding the energy of the incident neutrons. This work employed the Maximum Entropy Deconvolution (MAXED) unfolding algorithm. This Fortran 90 algorithm requires an a priori default spectrum, to which the algorithm applies a combination of response functions to statistically derive the experimental data by weighting the measured data to account for specified errors in measurement.[7]

Surrogate Vehicle Construction and Instrumentation with BSS and D-D Neutron Generator
A surrogate military vehicle was constructed, consistent with the legacy radiation transport experiments that frequently used metal boxes constructed of iron or steel.[2,3,6,10] *For our work, sheets of steel were mounted and bolted into an aluminum frame, as depicted in Figure 2. Aluminum was selected as the framing material due its low microscopic cross section for fast and epithermal neutron absorption. The frame was designed to permit easy replacement of the steel sheets with other materials and various sheet thicknesses. The three-inch diameter hole*

at the top of Figure 2 was positioned for instrumentation, so that a LiI(Eu) scintillator and photomultiplier tube could be inserted through the hole into the polyethylene Bonner spheres, in order to measure the spectrometer response inside the steel box, and the hole was sealed with borated polyethylene (BP) putty during in-box measurements; for free-field measurements, the box was simply removed. In both measurement configurations, aluminum stability rings and a laboratory jack were used to ensure identical positioning and orientation of the scintillation crystal, as shown in Figure 3. Finally, the entire experiment was enclosed by 4-inch slabs of BP for radiation shielding purposes.

An Adelphi DD108 Deuterium-Deuterium (D-D) neutron generator was positioned 24.1 cm from the steel box and served as a nearly isotropic source of 2.45 MeV mono-energetic neutrons. Measured BSS count rates and associated uncertainties for both the steel box and free-field configurations were input into the MAXED software, which produced the unfolded experimental solution spectra.[11] This same experimental geometry was replicated in MCNP6, including the BSS, steel box, accelerator head, and BP shielding. A graphic depiction of the input file geometry is shown in Figure 4 for both the steel box and free-field configurations. The LiI(Eu) scintillator was modeled in the same manner described by Mares and Schraube in their seminal paper from 1994 on BSS functionality.[12] The model utilized an aluminum right circular cylinder (RCC) enclosing a vacuum of 1.4 (diameter) × 1.6 (height) cm^2 to house the 4 (diameter) × 4 (height) mm^2 LiI crystal, which consisted of 5.18% ^{6}Li and 94.82% ^{127}I with a density of 3.84 g/cm^3. A schematic of the RCC scintillator model is shown in Figure 5. As discussed previously, all computational neutron spectra data were calculate using an F4 average neutron flux tally across the scintillator crystal, and thermal neutron scattering accounted for chemical binding and crystalline structure effects from the polyethylene through the S(α,β) treatment.

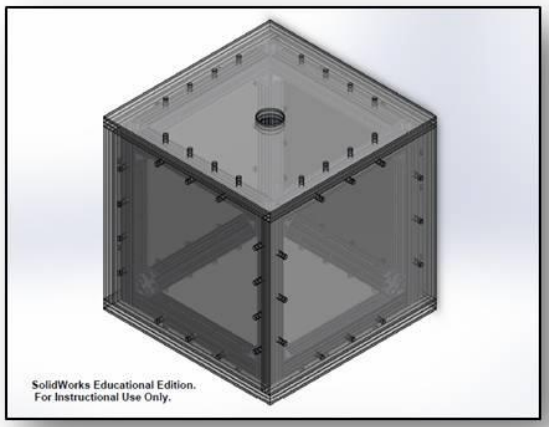

Figure 2. Schematic of the surrogate military vehicle testing apparatus, shown with the scintillator opening in the upward position. The steel plates are bolted to an aluminum frame during measurements.

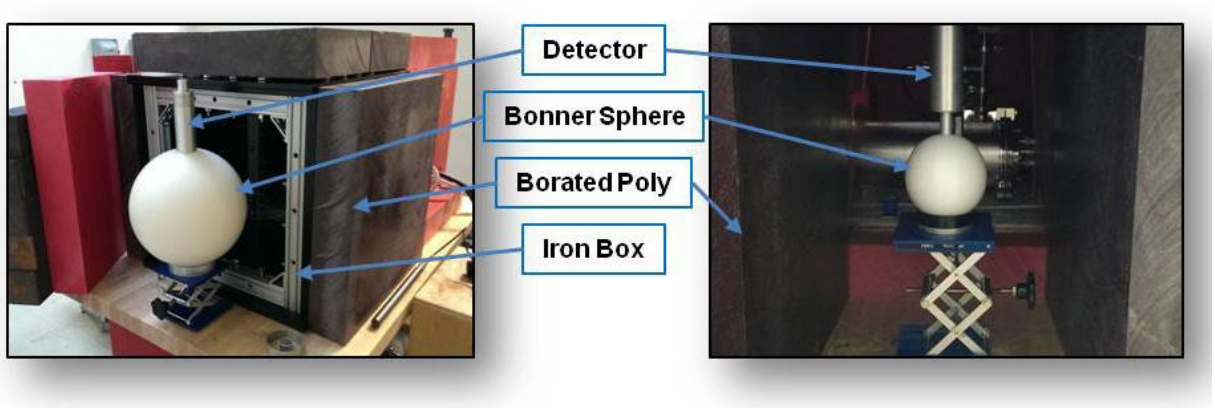

Figure 3. Experimental BSS apparatus. Left: orientation of the BSS prior to insertion into the steel box. Right: BSS employed in the free-field measurement configuration.

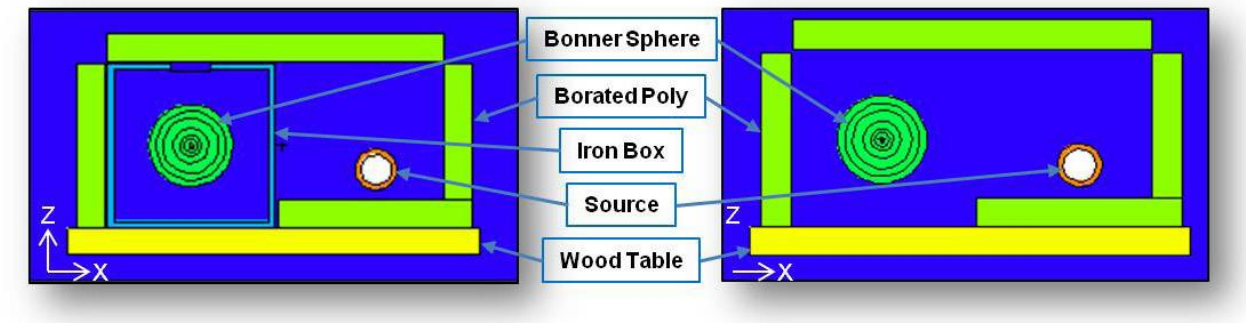

Figure 4. Side view of experimental geometry, as modeled in MCNP6. Left: steel box measurement configuration. Right: free-field configuration.

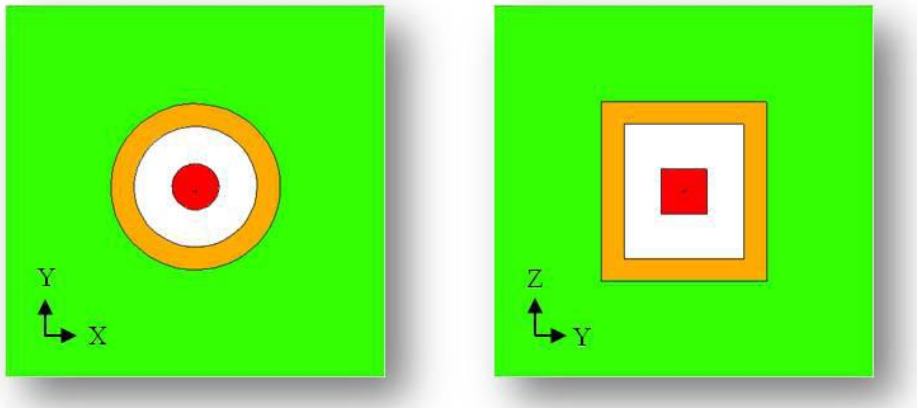

Figure 5. A schematic of the LiI(Eu) crystal modeled in MCNP6 using the technique employed by Mares and Schraube.[12] The crystal, modeled as an RCC (red) in the center of the image, is surrounded by a vacuum (white), and an aluminum RCC (orange) encases the vacuum. The entire structure is surrounded by polyethylene (green), as part of the BSS moderating spheres.

Neutron Protection Factor of a Surrogate Vehicle to D-D Neutron Source.

Figures 6 and 7 show the experimental (6) and MCNP6-computed (7) lethargy flux spectra within the steel box and free-field, when exposed to a 2.45 MeV mono-energetic neutron source located 24 cm from the surrogate vehicle. The MAXED solution spectra resulted in χ^2-values

of 0.86 and 0.91 per degree of freedom for the steel box and free-field, respectively, which indicate statistically significant agreement between the MAXED-generated solutions and the measured BSS count rates and associated uncertainties.

The structure and intensities of the steel box spectra in Figure 8 demonstrate reasonable agreement, except for the absence of these structures across the intermediate energy range of 10 eV – 500 keV. This discrepancy is likely attributable to the poor resolution of the BSS across those energy levels, where the BSS suffers from a lack of strong structures within the response matrix.[7] In Figure 7, the behavior of the experimentally measured free-field neutron lethargy flux spectrum is consistent with the MCNP6-computed spectrum, with a few notable differences. Specifically, discrepancies in intensity are evident between 1 to 2.45 MeV, which we attribute to the presence of high-energy neutrons that failed to down-scatter in the manner anticipated by MCNP6. Additionally, the experimental data are missing a structure at 0.5 MeV, which is also likely due to detector inefficiencies at that intermediate energy. Also, for both the iron box and free-field configurations, we have not yet improved the fidelity of our modeled geometry, or improved upon our initial variance reduction methods, so other explanations for the observed disparities are certainly plausible. Despite each observed inconsistency in the specified energy range, the MCNP6-computed lethargy flux spectra largely agree with the experimentally-observed spectra, and all spectra correctly predict that the highest frequency of detected neutrons would be observed in the thermal region and the 2.45 MeV energy level.

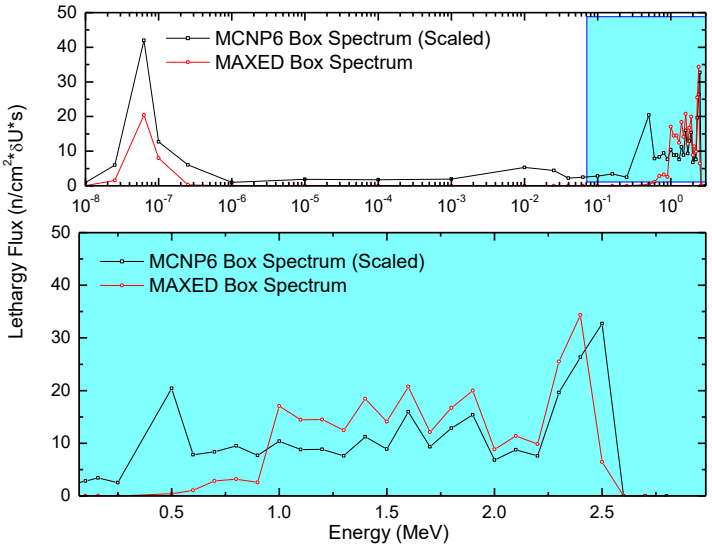

Figure 6. Experimental (red) and MCNP6 (black) D-D neutron spectra, in units of lethargy flux, within the surrogate vehicle. The spectra were obtained from a LiI(Eu) scintillation detector inside a BSS and unfolded using MAXED, which resulted in a χ^2-value of 0.86 per degree of freedom.

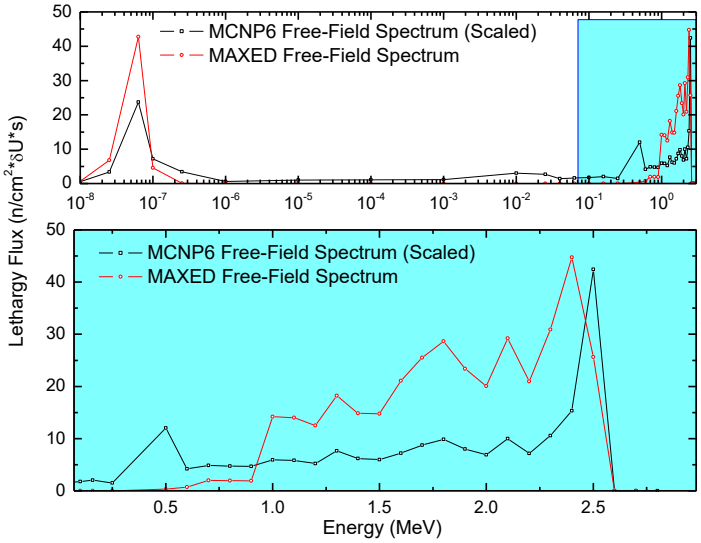

Figure 7. Experimental (red) and MCNP6 (black) D-D neutron spectra, in units of lethargy flux, for the free-field configuration. The spectra were obtained from a LiI(Eu) scintillation detector inside a BSS and unfolded using MAXED, which resulted in a χ^2-value of 0.91 per degree of freedom.

5.1.1.2 Task 2

#	Material (S/C)	Geometry (S/C)	Source (Mono/Poly)	Spectra
2	S	S	Mono	Gamma

The following text, images, and data were presented as:
W. Erwin, J. Clinton, J. McClory, B Singleton, "Verification and Validation of Monte-Carlo N-Particle 6 (MCNP6) for Computing Gamma Protection Factors," poster presentation delivered at the 2015 Hardened Electronics and Radiation Technology Technical Interchange Meeting in Chantilly, VA on 23 April 2015.

Experimental and Modeling Methodology:
The primary experiment for this investigation was a simple comparison of dose deposited by ^{137}Cs photons in a NaI detector in a shielded and un-shielded enclosure. These two measurements were then modeled in MCNP6 and compared to the experimental results. The criteria for passing validation was a modeled GPF confidence interval entirely bounded within 5% of the experimental GPF. Radioisotopes were used to produce a nearly isotropic source of mono-energetic photons at 662 keV. A sodium iodide detector measured the spectrum and activity 41 cm away from the source. Then a detector was placed inside a hollow steel box, as shown in Figure 1, and the detector measured the spectrum at the same distance from the source. These two configurations were then modeled in MCNP6, and the resulting experimental GPF was compared to the modeled GPF.

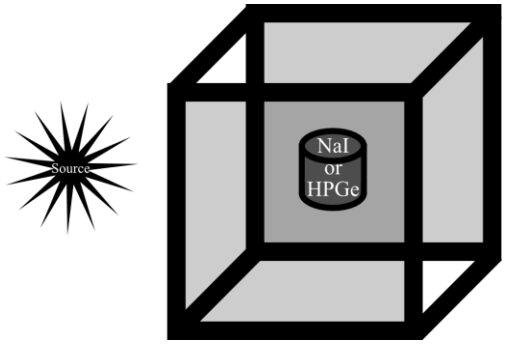

Figure 1. Diagram of the validation experiment, not to scale.

The MCNP6 input deck was then modified multiple times in order to determine the fidelity required to achieve a modeled GPF within 5% of the experimental GPF. The geometric modifications included varying the inclusion and/or complexity of various components of the box, testing apparatus, and nearby objects. Other modifications included varying the precision of the modeled material and geometry, accounting for moisture in the air, and varying the number of tracks to be evaluated.

The validation experiment was then repeated with several variations. These variations included the number, type, and placement of the source, and the thickness of the steel enclosure. These experiments were then compared with corresponding MCNP6 models.

Results and Discussion

The model spectra showed the same features in the same places as the experimental spectra, as shown in Figure 3.

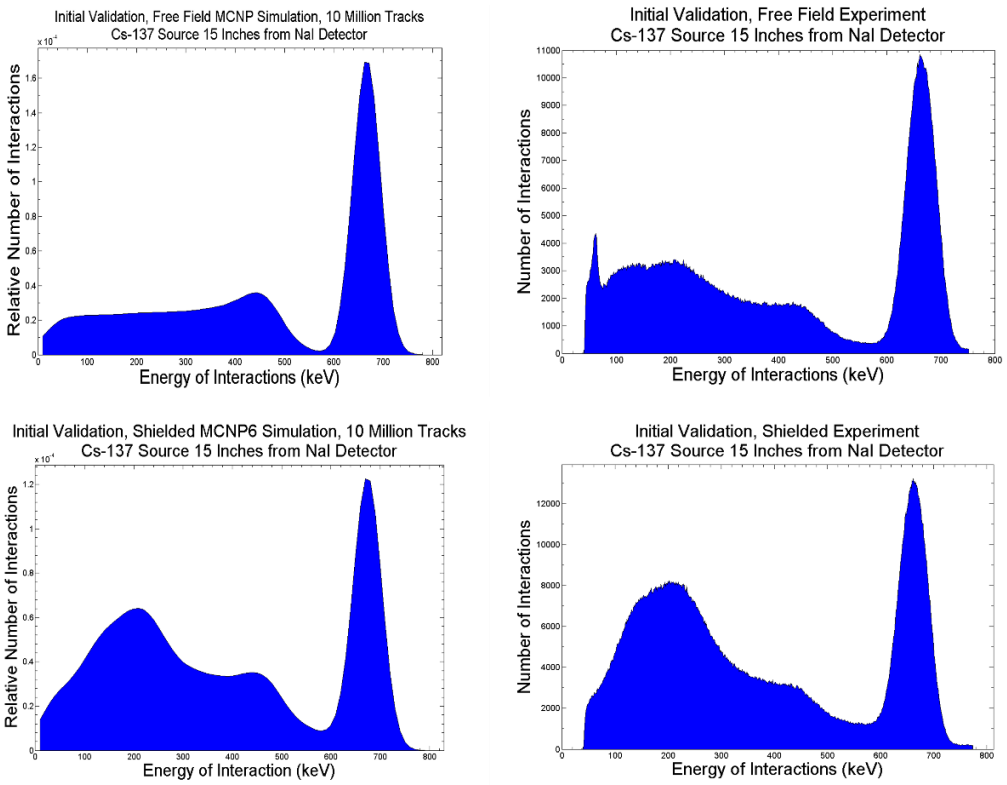

Figure 3. Simulated (left) and experimental (right) spectra for the shielded and unshielded configurations. The simulated spectrum was convoluted with a point-spread function to generate an ideal NaI response. The experimental results did not include the lowest energy bins, as these tended to become saturated with electronic noise.

The fidelity study's results confirmed the importance of three dimensional models and sufficiently large numbers of evaluated particles. However, material fidelity had no significant effect on the overall results. A model with only a single isotope of the most-common element in a material produced no statistically significant differences from a model containing all naturally occurring isotopes of all elements present in a material. This is due to the mechanics of photon interactions with matter, which are driven primarily by the number and density of charged particles present in a material, and not their specific configurations.

Several alternate models provided useful comparisons for verifying MCNP6 results. However, none combined the fast run time, three-dimensional modeling, versatility, or simple input file structure of MCNP6. MCNP6 was also verified by comparison with theoretical radiation attenuation and Compton scattering models as an excellent choice for this application.

5.1.1.3 Task 3

#	Material (S/C)	Geometry (S/C)	Source (Mono/Poly)	Spectra
3	S	S	Poly	Neutron

The following text, images, and data were published as:
A.W. Decker, S.R. McHale, J.A. Clinton, J.W. McClory, M. Millett, "Verification and Validation of MCNP6.1 Neutron Protection Factor Estimates Using the WSMR Fast Burst Reactor," *Journal of Radiation Effects, Research and Engineering*, vol. 35, no.1, pp. 52-58, Apr. 2017.

Experiment

The purpose of this research was to further verify and validate (V&V) MCNP6.1-generated Neutron Protection Factor (NPF) estimates for a steel box, by extending prior successful work with a mono-energetic source [5] to new investigations using a complex neutron source spectrum. The 235U fission neutron spectrum for this experiment was generated by the FBR at WSMR. The previous, monoenergetic experiment and the research reported here employed a steel box with sides of 61 cm and wall thicknesses of 2.54 cm.

Experimental Design

A steel box was used as a surrogate military vehicle, consistent with the legacy radiation transport experiments using boxes constructed of iron or steel [2], [5]. The steel plates were mounted and bolted onto an aluminum frame, as depicted in Fig. 2. Aluminum was selected as the framing material due to its low microscopic cross section for fast and epithermal neutron absorption. The three-inch diameter hole shown in Fig. 2 enabled the insertion of the LiI(Eu) scintillator and photomultiplier tube into the steel box and polyethylene Bonner spheres, which allowed measurements of shielded spectrometer responses within the steel box. During shielded measurements, a portion of the photomultiplier tube partially filled the hole in the top of the steel box, leaving a 1.27 cm gap around the circumference of the tube. This gap was filled with borated polyethylene putty to prevent thermal neutrons from entering the box and influencing the detector response. During unshielded measurements, the steel box was simply removed.

In both measurement configurations, aluminum stability rings and an aluminum laboratory jack were used to ensure consistent positioning and orientation of the scintillation crystal across all measurements. In both shielded and unshielded experiment configurations, the LiI(Eu) scintillator was positioned at a horizontal distance of exactly 12 ft from the middle of the FBR and centered vertically with the FBR. The experimental instrumentation was shielded from the high-flux environment of the FBR by a steel, lead, and polyethylene enclosure located near the experiment.

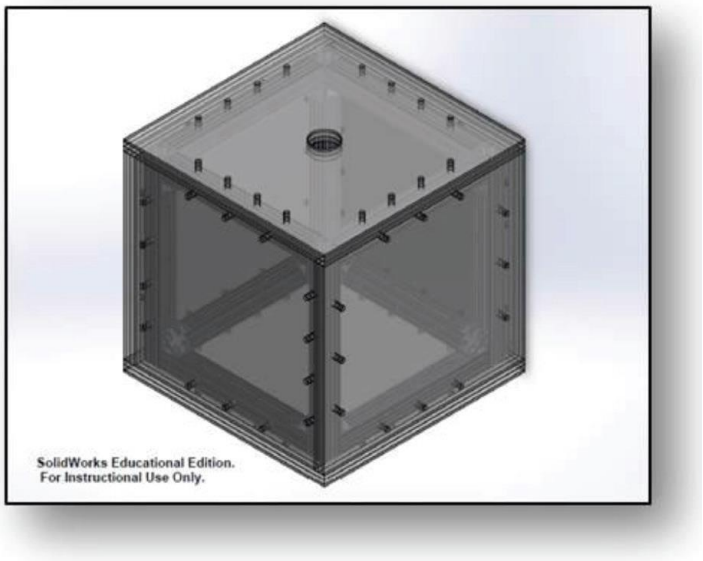

Figure 2. Schematic of the surrogate military vehicle testing apparatus, shown with the scintillator opening in the upward position. The steel plates are bolted to an aluminum frame during measurements.

Measured BSS count rates and associated uncertainties for both the shielded and unshielded configurations were input into the MAXED software, which produced the unfolded experimental solution spectra. Spectra values were then normalized to facilitate comparison against the computational neutron flux spectra data.

Computational Design

This experimental geometry was replicated in MCNP6.1, including the steel box and instrumentation enclosure. Fig. 3 provides a "top-down" depiction of the input file geometry for the shielded configuration.

The FBR was modeled as a point source using the 235U fission energy spectra computed previously by FBR staff and available from their office. The source was collimated into a directional cone with a half-angle of 41° and directed toward the steel box, which ensured neutron interactions with all layers of the modeled instrumentation enclosure. The shielded detector response to the neutron spectrum was computed at a position in the steel box identical to that described in the previous section, and the unshielded response to the spectrum was simulated at the same position in the absence of the steel box. S(α,β) treatment was utilized to account for thermal neutron scattering due to the chemical binding and crystalline structure effects from the polyethylene in the instrumentation enclosure. The MCNP6.1 computed neutron flux spectra served as the a priori input into MAXED to assist in spectra deconvolution.

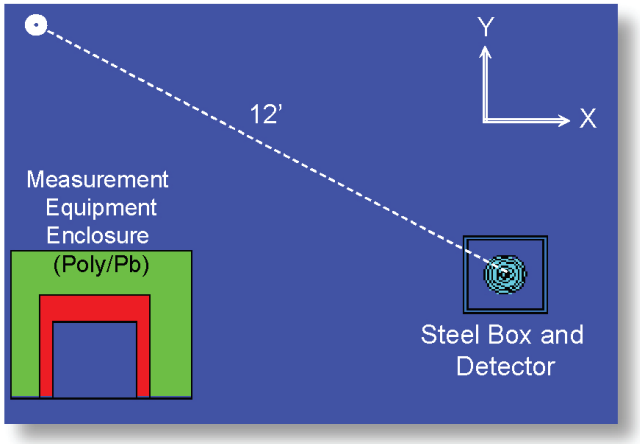

Figure 3. Top-down view of the experiment geometry, as modeled in MCNP6.1. Dark blue represents air, while light blue is the steel box, green is the polyethylene, and red is lead.

All computational neutron spectra data were calculated using an F4 average neutron flux tally across a 12 in diameter sphere of air located in place of the largest Bonner sphere; the Bonner spheres were not modeled as polyethylene. Both the shielded and unshielded MCNP6.1 neutron spectra were normalized to facilitate comparison against the experimental flux spectra data.

Results and Analysis

Shielded Spectra Results

Fig. 4 shows the BSS-measured and MCNP6.1-simulated spectra within the steel box and in the presence of the ^{235}U neutron source generated by the FBR at WSMR. The spectra demonstrate good overall structural and intensity agreement, especially above 100 keV. As anticipated, the MAXED results suffered from low resolution inherent in the BSS across intermediate energies, which is likely responsible for the disparity in intensity across that energy region. Additionally, the experimental results demonstrated higher than expected neutron flux intensities between 0.1 - 5.0 eV, which may be attributable to the borated putty used to preclude excessive thermal neutron counts.

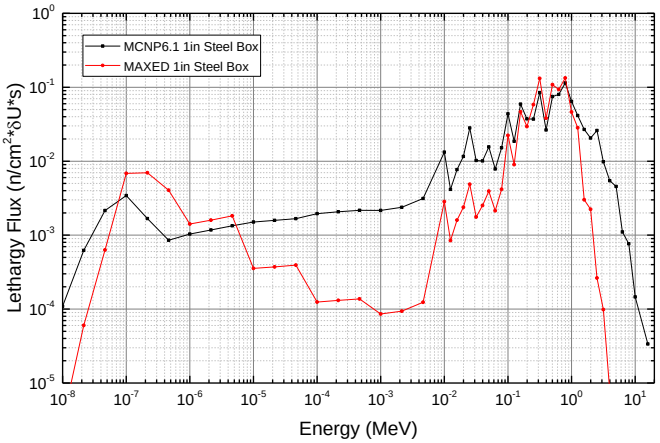

Fig. 4. Neutron spectra from the ^{235}U neutron source at the WSMR FBR as measured by a BSS within the steel box (red) and computed by MCNP6.1 (black) in units of lethargy flux.

Despite these discrepancies, the neutron spectra share a similar shape and relative intensities anticipated for a ^{235}U fission source. The MAXED solution χ^2/df-value was 0.70, which indicated the solution spectrum matched the experimental data within the measurement error tolerances to a statistically significant degree. Based upon these factors, both spectra are deemed valid approximations for the neutron flux spectrum present within the Steel Box during exposure to the FBR.

Unshielded Spectra Results

Similarly, the unshielded neutron spectra demonstrate good overall structural and intensity agreement, specifically across energy regions above 100 keV. As shown in Fig. 5, the same BSS low resolution effects are again present, as well as the expected peaks in neutron lethargy flux for a measured ^{235}U fission source.

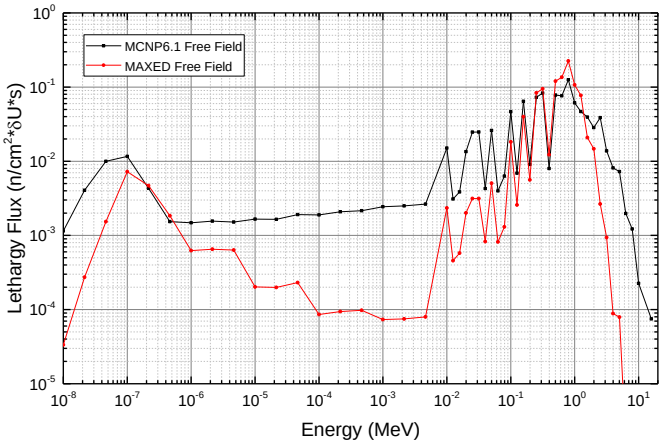

Fig. 5. Neutron spectra from the ^{235}U neutron source at the WSMR FBR as measured by a BSS in the unshielded configuration (red) and computed by MCNP6.1 (black) in units of lethargy flux.

The MAXED solution χ^2/df-value was 0.79, which indicated the solution spectrum matched the experimental data within the measurement error tolerances to a statistically significant degree. Based upon these factors, both free-field spectra are deemed valid approximations for the neutron flux present at a distance of 12 ft from the FBR.

Spectra Comparison

Both the computational and experimental unshielded solution spectra were compared against measured FBR neutron flux spectra recorded at various distances from the core, which is shown in Fig. 6. A comparison of these spectra suggests that the high energy oscillations present in both the experimental and computational unshielded spectra may likely be attributed to neutron interactions with the instrumentation enclosure, which was required during the physical experiment. This structure was not present within the FBR chamber during any of the WSMR spectra measurements, which were recorded using foil activation analysis.

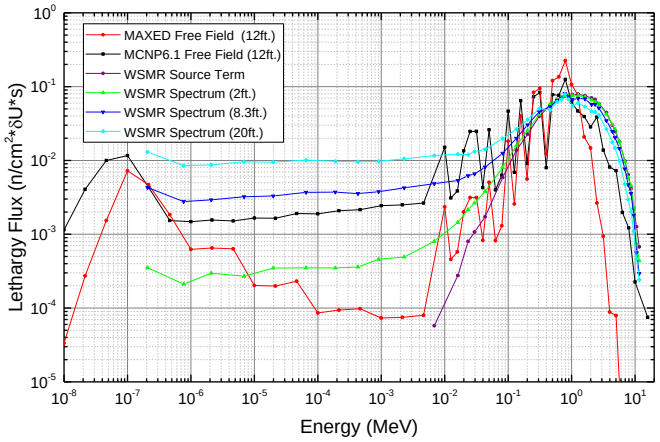

Fig. 6. Comparison of the unshielded neutron spectra, both computational (black) and experimental (red), against plotted WSMR data of neutron flux from the FBR at various horizontal distances.

The demonstrated agreement in energy peak location and the overall spectra shape congruency suggests that both solution spectra accurately depict the FBR neutron emission.

5.1.1.4 Task 4

#	Material (S/C)	Geometry (S/C)	Source (Mono/Poly)	Spectra
4	C	S	Mono	Neutron

The following text, images, and data were submitted for publication as:
J.D. Glesmann, M.G. Millett, M.E. Nelson, "Measurement and Model Validation of Neutron Protection Factors with a D-T Neutron Generator," Submitted to the Journal of Radiation Effects, Research and Engineering, vol. 35, 2017.

Computational Approach (MCNP6)

To validate the measured NPFs in this work, MCNP6 models were developed for each experimental configuration including the neutron generator, BSS, the vehicle surrogate boxes, and the accelerator room's concrete walls. The neutron generator produces essentially mono-energetic neutrons, but many source neutrons undergo scattering interactions in the wall and return to the exposure location as room return. These room return neutrons contribute significantly to the neutron energy distribution at the exposure location, so they must be accurately modeled. The model simulates flux, dose equivalent, and detector response for each experimental configuration, free field and shielded. Model validation is primarily based on a comparison of measured NPF and simulated NPF, but comparisons with hand calculations based on published neutron cross sections are also used.

Figure 1 below shows the USNA Neutron Generator Facility in the basement of Rickover Hall. Outside the neutron generator cell is a control room where a technician can operate the generator and its ancillary equipment. A wooden door allows entry into the generator cell, and is lined with a layer of lead for shielding. The generator cell contains the neutron

generator and the detection and cooling support systems. The generator is placed on an aluminum stand approximately 137.5 cm above the ground.

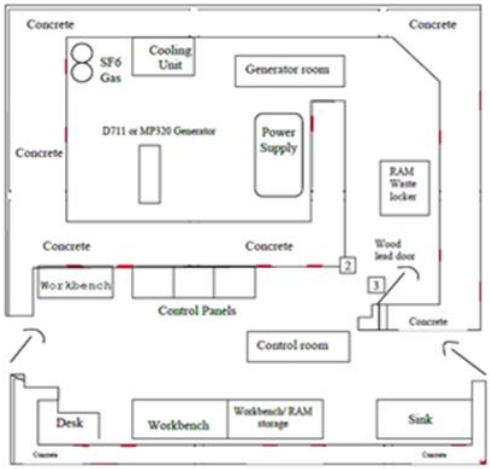

Fig. 1. USNA Neutron Generator Facility schematic.

Experimental Approach (BSS and Unfolding)

The experimental instrumentation chosen to evaluate the flux within the surrogate cell was the Bonner Sphere Spectrometer (BSS) [9]. The BSS consists of six Bonner spheres varying in diameter, totaling seven configurations including bare. The full detection system and instrumentation assembly consisted of one of the seven BSS configurations, a lithium iodide detector, a signal processing unit, and a computer used for data acquisition. Figure 2 shows the manufacturer product photo of the BSS with five Bonner spheres, but does not include the entire detection system. The NPF experimentation done at USNA used all seven BSS configurations to produce the neutron spectrum.

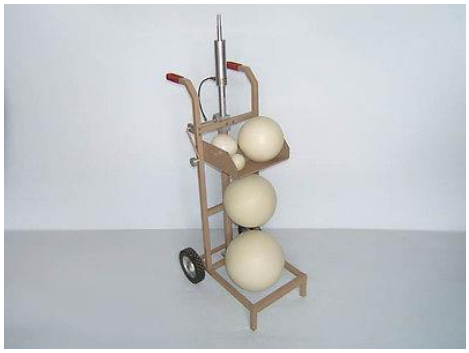

Fig. 2. Bonner Sphere Spectrometer detection system.

The six Bonner Spheres used for the NPF experiment consisted of diameters of 2", 3", 5", 8", 10", and 12" [9]. Each Bonner Sphere contains a center well, into which a europium doped lithium iodide scintillator is placed (the detector is located at the center of the Bonner sphere). A stepped well in the larger spheres accommodates the detector's photomultiplier tube (PMT). Figure 3 shows a Bonner sphere being used for free field measurements within the USNA neutron generator room, with the lithium iodide detector inserted and the PMT held vertically

above the sphere. Height of the detector was held consistent by using aluminum rings and an aluminum jack stand (shown). The detector was maintained along the axis of the neutron generator.

Fig. 3. Location of source in reference to the detector.

Experimental neutron spectra were determined using UMG v 3.3 unfolding software. UMG v 3.3 (Unfolding with MAXED and GRAVEL) is a computational package written for the analysis of data measured with spectrometers that require the use of unfolding techniques. The package offers two different means of unfolding: MAXED applies the maximum entropy principle to the unfolding problem, and GRAVEL uses a modified SAND-II algorithm to do the unfolding. Each approach offers a "few-channel" and a "multi-channel" option. For this work, the MAXED few channel option was used [10, 11].

Experimental Results

Figure 4 shows the results of the unfolded spectra converted to dose equivalent received from both the free field and vehicle surrogate configurations. The blue and red histograms give the dose in pico-Sieverts (pSv) per source neutron for the free field vehicle surrogate versus neutron energy. The green histogram also depicted in Figure 4 is the neutron quality factors (NQFs) plotted versus neutron energy by Hertel and Veinot [12]. These quality factors were determined to be the best choice for flux to dose conversion factors because they are both current and defined over specific energy bins rather than pointwise, supporting the conversion of a continuous spectrum to dose. Other flux to dose conversion factors were considered but not used, primarily because they were not continuous [13, 14]. In Figure 4, the energy dependence of both the shielded and unshielded dose and the NQFs is clear. The shape of the NPF curve is significant because the NQFs are relatively constant across a region that includes the source neutrons, and those slowed by passage through the surrogate vehicle (represented by a downward shift in the energy of the return peak above 1 MeV). The implication of this NQF characteristic related to the 14 MeV source neutrons, is that the resulting NPF value is expected to be low for the combination of a 14 MeV source and the selected surrogate vehicle. In other words, while the surrogate vehicle may provide shielding against thermal neutrons, the effect of the vehicle on dose from neutrons above 1 MeV may not be intuitive, and may even result in a reverse shielding effect.

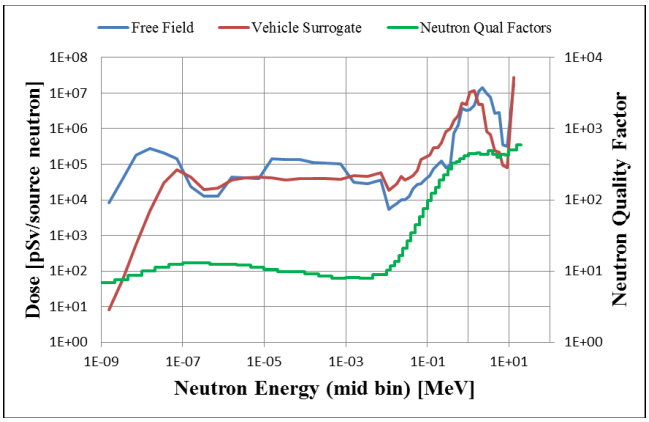

Fig. 4. Unfolded (measured) dose spectra and neutron quality factors

Computational Results

The facility indicated in Figure 1 was defined in terms of a MCNP6 model, and Figures 5 and 6 show the top and side views of the modeled configuration. These figures were created using MCNP's internal Visual Editing software. The color schemes on each of the figures are representative of the materials defined in the model.

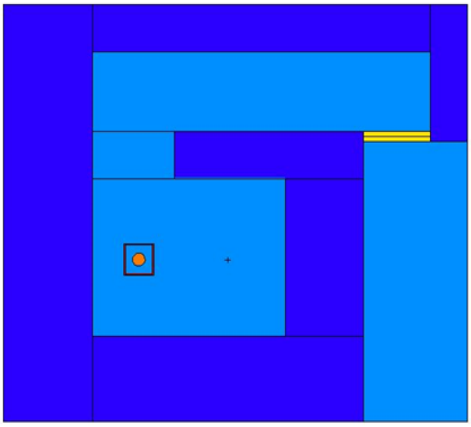

Fig. 5. MCNP6.1 Visual Editor output for the neutron generator facility in the XY plane (top view)

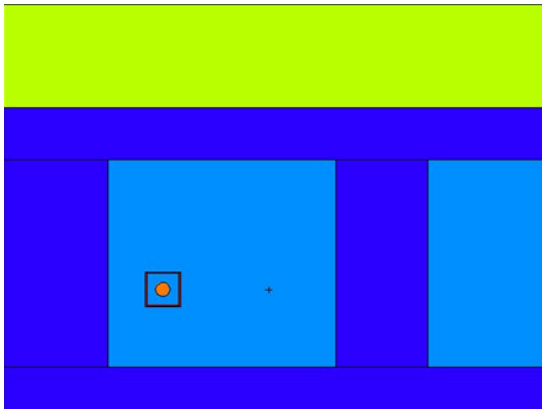

Fig. 6. MCNP6.1 Visual Editor output for the neutron generator facility in the XZ plane (side view)

Similar to Figure 4, Figure 7 shows the results of the computational (simulated) spectra converted to dose equivalent received from both the free field and vehicle surrogate configurations. Similar to Figure 4, the x-axis is the neutron's upper bin energy in units of MeV and the y-axis is the whole body dose received in pSv per source neutron.

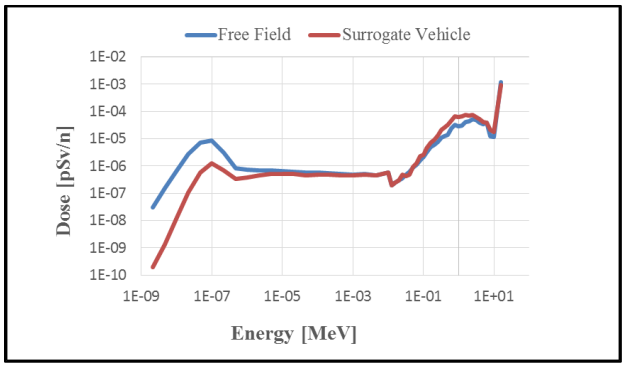

Fig. 7. Computational dose spectra results produced by MCNP for free field and surrogate vehicle configurations.

In Figure 8, the experimental and computational dose spectra for each configuration are normalized for comparison. Each of the dose spectra follow similar characteristics, thus are indicative of agreement.

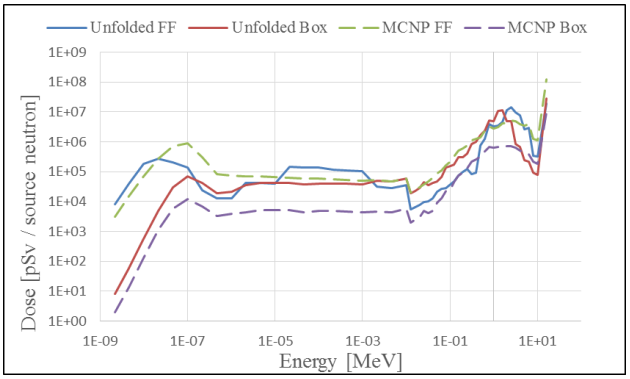

Fig. 8. Comparison of computational and experimental dose spectra.

5.1.1.5 Task 5

#	Material (S/C)	Geometry (S/C)	Source (Mono/Poly)	Spectra
5	C	S	Mono	Gamma

The following text, images, and data were published as:
T.J. Gates, C.R. Zeigler, C. Bouvier, A.W. Decker, "Verification and Validation of MCNP6.1 for Gamma Protection Factor Estimates of an Armored Box," *Journal of Radiation Effects, Research and Engineering*, vol. 35, no.1, pp. 76-82, Apr. 2017.

Experimental Design

The surrogate armored vehicle consisted of aluminum framing which supported panels of ½ in steel, ½ in glass reinforced plastic (GRP), and ¼ in aluminum. When assembled, this formed

a 2ft^3 hollow armored box, which provided a simplified but effective ballistic armor for analysis. Specifically, the inner-most layer of steel simulated high-density metallic armor, the middle layer of GRP provided an anti-spallation liner, and the outer-most layer of aluminum simulated the vehicle skin.

Additionally, all three top plates of the armored box were designed with a 3-in hole through their center. This hole allowed detector cabling to pass out of the box during shielded measurements, once all the plates were affixed. Assembly of the box can be seen in Fig. 1, and a very similar box schematic is provided in Fig. 2, with the only difference being the number of holes used to affix the plates to the internal frame.

Figure 1. The armored box included an 80/20 aluminum frame, which held in place the three layers of armor: steel, GRP, and aluminum. Together these layers replicate basic ballistic armor found on U.S. Army vehicles.

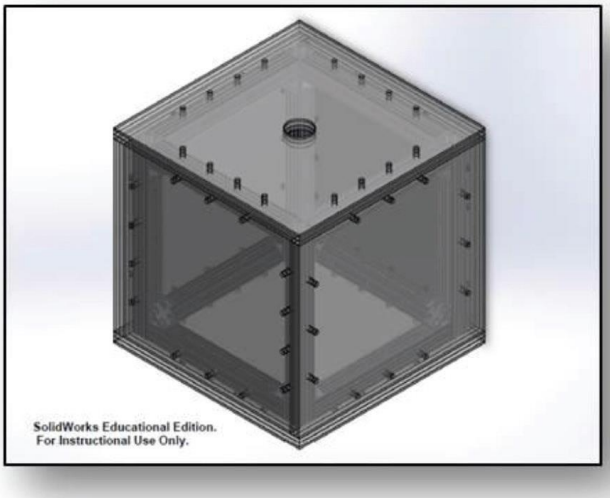

Figure 2. Schematic of the armored surrogate military vehicle, shown with the 3-in detector opening in the upward position. The armor plates are bolted to an aluminum frame during shielded measurements; however, only eight screw holes were present on each side of the box used in this experiment.

For the shielded measurement, a 5 μCi 137Cs source was centered on one box face at a distance of 10 cm from the outermost surface. The emitted gamma ray spectrum was measured using a 16 in × 4 in × 2 in NaI scintillator detector, which was placed upright and centered inside the box. The 16 in × 4 in side of the detector faced the source to maximize the source-detector solid angle. This experimental design for the shielded gamma ray measurement is depicted in Fig. 3, except the closest layers of armor are removed to allow a view of the detector.

The unshielded measurement was designed to mirror the shielded experiment as nearly as possible but without the surrogate vehicle present. The NaI detector was held vertical using an aluminum lab stand and clamp, and 1¼ in layers of paper were stacked and placed under it to maintain consistent placement with the shielded measurement. Source location and strength remained unchanged from the previous shielded measurement. Fig. 4 depicts the unshielded experimental configuration.

For both configurations, a calculated dose rate was determined from measured counts across 2000 energy bins. These values were adjusted for detector dead time before calculations of total absorbed dose in the crystal were performed, thereby allowing a final calculation of dose rate deposition in units of Gy/s.

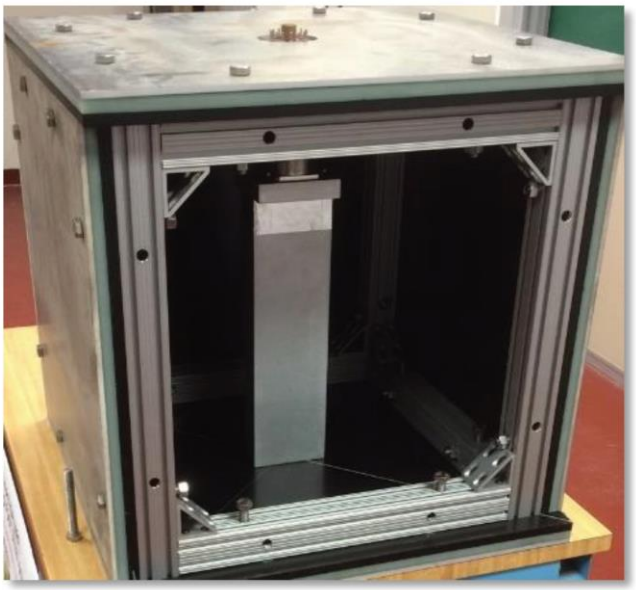

Figure 3. Experimental design for the shielded gamma ray measurement. Of note, the missing layers of armor were replaced prior to spectrum measurement, but they are removed here to provide a view of the detector. As shown, the 16 in × 4 in × 2 in NaI scintillator detector was placed vertically and centered within the box during measurements, and the top of the detector can be seen protruding through the 3-in hole at the top. The ^{137}Cs source was placed on the far side, centered on the box, at a distance of 10 cm from the surface.

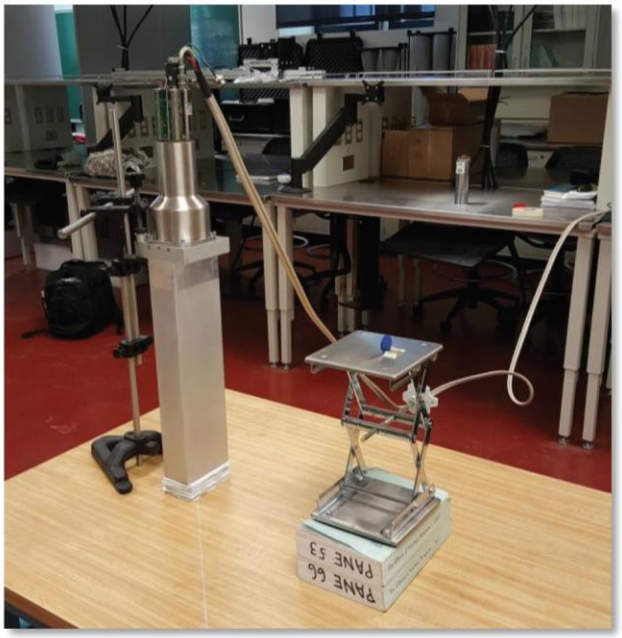

Figure 4. Experimental design for the unshielded gamma ray measurement. As shown, the 16 in × 4 in × 2 in NaI detector was placed vertically and supported by 1¼-in layers of paper. The 137Cs source was placed identically on the far side, centered on the box, at a distance of 10 cm from the surface.

Background measurements were recorded for both configurations and subtracted from the measured data to provide cleaner spectra. Additionally, sufficient counts reduced experimental error below 0.2%, and detector efficiency was also tracked to ensure dead time remained below 3%. Using these values, measured dose rate uncertainties for both configurations were calculated, and these values were propagated forward in the final calculation of GPF error.

Computational Design

Surface cards were defined within MCNP6.1 according to dimensions measured during experimentation. Most geometries were rectangular parallel pipettes (RPPs). A sphere about the origin of the coordinate system was set at 10 m, outside of which the photon importance was set equal to zero. Cell cards were defined for all materials, including aluminum, GRP, steel, air, concrete, wood, and the NaI detector crystal, and all were assumed to be homogenous materials. Of note, the hollow steel legs of the wooden table were neglected in the simulation, as well as the aluminum stand supporting the source, the photomultiplier tube, and the instrumentation cables. The model did not account for bremsstrahlung or coherent scattering. Energy bins and desired output tallies were identified in the data cards, and material compositions were defined for the materials mentioned above. All materials were associated with the most recent photon cross section libraries available in MCNP6.1. Fig. 5 illustrates the basic computational design for the shielded simulation.

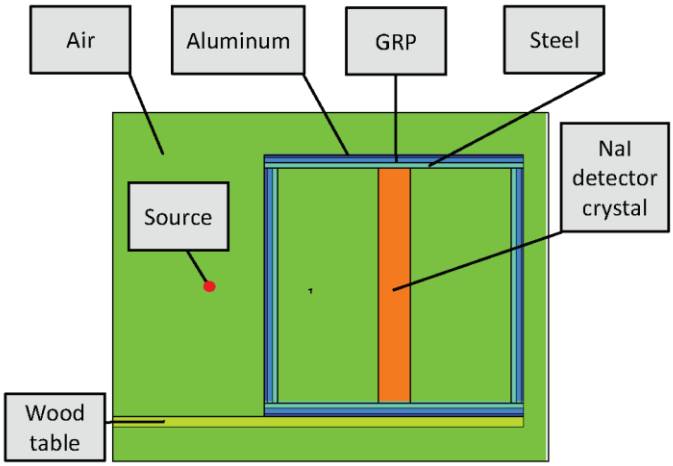

Figure 5. Computational design for the basic shielded gamma ray measurement. A 16 in × 4 in × 2 in NaI crystal was simulated within the box and both F6 and F8 tallies were utilized to evaluate gamma interactions within the crystal. A simulated 137Cs source located 10cm from the box provided the gamma flux.

Results and Analysis

Experimental Analysis

Plots showing the experimental data are provided in Fig. 7. Red indicates the unshielded data, while blue represents data from the basic shielded configuration within the armored box.

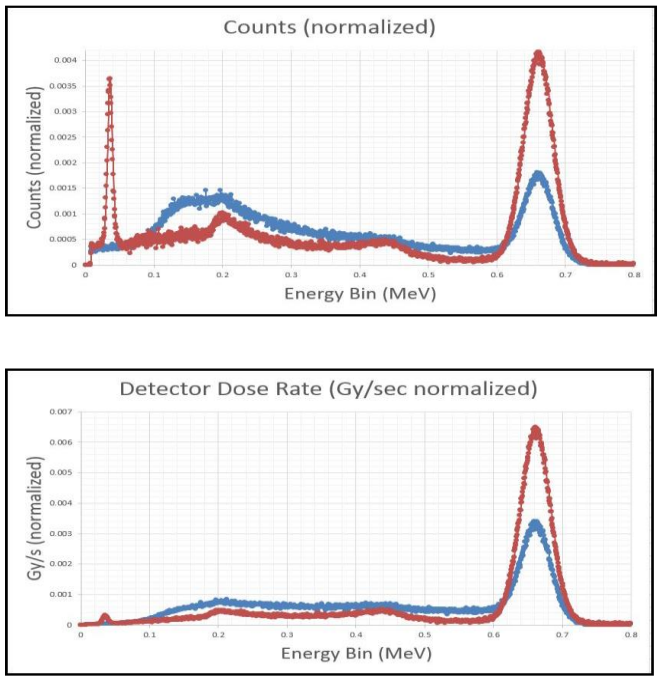

Fig. 7. Excel plot of the experimentally-measured gamma spectra using a NaI detector. Red indicates data from the unshielded configuration, while blue represents the shielded data.

The higher number of counts and the increased dose rate present in the lower energy region of the unshielded data was likely due to down-scattering of higher energy photons from

interactions with the shield material layers. However, at higher energy regions around 662 keV, significantly lowering count rates are reported due to the shielding attenuation. Therefore, the data presented is Fig. 7 is logical, and data analysis resulted in a measured GPF value of 1.46 ± 0.01 for the armored box.

Computational Analysis

The computationally-derived data provided similar graphs of spectra when plotted. Fig. 8 shows both the normalized F6 Tally (counts) and F8 Tally (dose rate). These graphs were enhanced to reveal spectra disparity at lower energy regions, which produces a similar trend in data to those measured experimentally. These data resulted in a MCNP6.1-derived GPF estimate of 1.53 ± 0.01 for the armored box in the basic configuration. As shown in Fig. 8, one limitation of this study is that the simulated detector response did not incorporate peak broadening based upon the physical detector response; however, this will be included in future work to improve dose estimation.

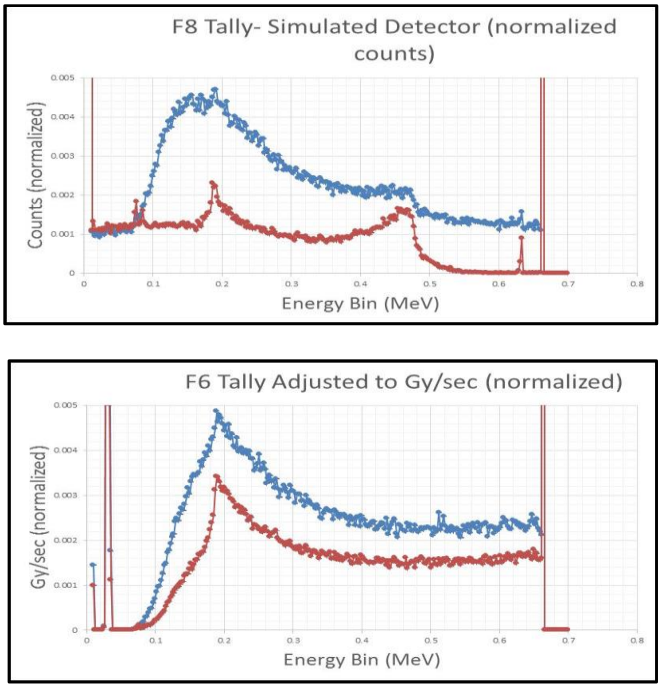

Fig. 8. Plot of the MCNP6.1-derived gamma spectra. Red indicates data from the unshielded configuration, while blue represents the shielded data. Of note, the simulated detector response does not take into account the resolution (FWHM) of the physical detector.

5.1.1.6 Task 6

#	Material (S/C)	Geometry (S/C)	Source (Mono/Poly)	Spectra
6	C	S	Poly	Neutron + Gamma

The following text, images, and data were published as:

W.J. Erwin, E. Cazalas, J.W. McClory, A.W. Decker, "Development of Radiation Protection Factors with Gamma and Neutron Spectroscopy using a Plutonium-Beryllium Source," *Journal of Radiation Effects, Research and Engineering*, vol. 36, no.1, pp. 88-94, Apr. 2018.

Results and Discussion

A 5 Ci PuBe source (provided and calibrated by Monsanto Research Corporation) produced the mixed neutron/gamma field with LiI and LaBr detectors for neutron and gamma measurements, respectively. Detectors were placed ~31 cm from the PuBe source. For a free-field measurement setup, detectors are placed in open air, approximately 1.2 m above the ground. In a shielded setup, the detectors were then placed within a cubic enclosure measuring 62.2 cm on each side as in Fig. 1.

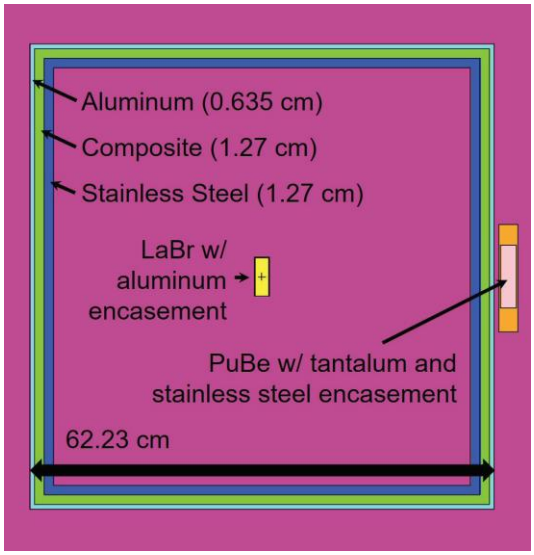

Figure 1. The geometry of the MCNP model in air including the composition and thicknesses of shielding material, inner detector, and PuBe source. The geometry is to-scale for the experimental shielding setup excluding walls, ceiling, and floor. Geometry and material makeup of the PuBe source is included from specification sheets provided by the manufacturer(Monsanto Research Corporation).

The results of experiment and simulation are shown in Fig. 2 and show a close match between the two up to 4.5 MeV. Although gamma rays above these energies may be produced by fissions within the PuBe source, these constitute a small minority of fission emissions, and fissions within the source happen at much lower rates than the reactions producing 4.5 MeV gamma rays; therefore, significant activities above this energy are not associated with established PuBe emission spectra [11]. Measurements taken with the source removed show no activity in this energy region, and the dead time divided by the live time for these measurements was 1%; pulse pileup is a function of this ratio [12]. This suggests that the higher-energy discrepancies are likely due to pulse pileup. Pulse pileup occurs when two photons deposit energy into the detector active region within the same pulse length measurement period (cumulatively defined as the detector dead-time).

Pulse pileup and neutron interactions cause the extension of experimental spectra into energy regions higher than source emission line at 4.43 MeV. The MCNP6 code executed here does not calculate pulse pileup, the lack of which is shown at energies higher than ~5 MeV and in the energy region lower than ~2.5 MeV in Fig. 2a). However, this does not alter the dose

contribution provided by the MCNP6 F8 tally as total energy is still deposited into the detector in the simulation. The simulation assumes the gamma line source emission in Fig. 2a) is created by the decay of the first and most probable excited nuclear state of the $^{12}C^*$ nucleus (4.43 MeV) created in the $^{9}Be(\alpha,n)^{12}C^*$ reaction [11]. Also included are the prevalent gamma decays (at lower energies) of ^{240}Pu and ^{241}Pu [13]. The dose contributions from the spectra are shown in Fig. 2b). As expected, dose contribution is significant where there are high bin counts at higher energies. The dose contribution due to pulse pileup at energies E > ~6 MeV are smaller and, thus, not shown in Fig 2b).

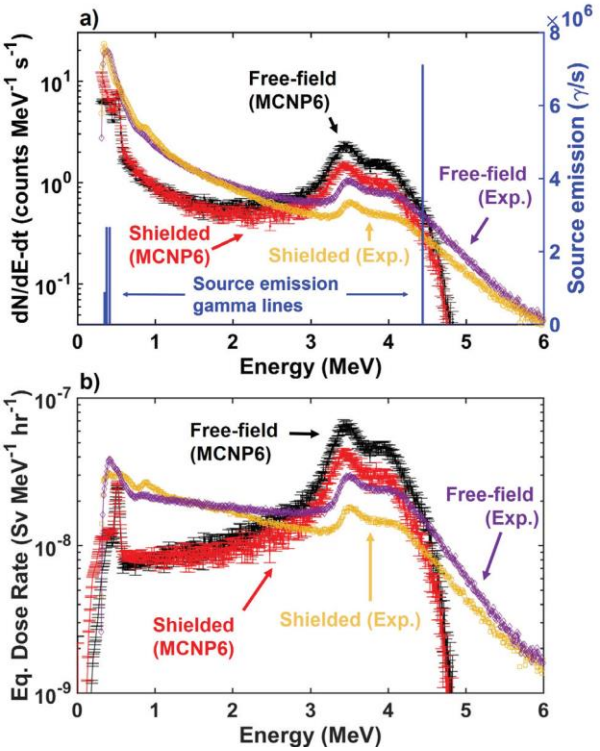

Figure 2. a) Comparison of experimental (Exp.) scintillation detector spectrum to MCNP6 simulation (MCNP6 with standard errors) with an F8 tally shows good matching of spectral features. b) The equivalent dose rate shows the importance of the contribution in regions where high bin counts occur with higher energy. For example, the high bin counts for bins with energy E < 1 MeV contribute less toward dose than may be perceived in a). At higher energies, E > 6 MeV, contribution to dose is also less due to low bin counts.

5.1.1.7 Task 7

#	Material (S/C)	Geometry (S/C)	Source (Mono/Poly)	Spectra
7	C	S	Poly	Neutron

The following text, images, and data were published as:
A.W. Decker, S.A. Heider, S.R. McHale, J.A. Clinton, J.W. McClory, M. Millett, "Verification and Validation of MCNP6.1 Neutron Protection Factor Estimates of an Armored Vehicle Surrogate Using the WSMR Fast Burst Reactor," *Journal of Radiation Effects, Research and Engineering*, vol. 36, no.1, pp. 65-71, Apr. 2018.

Experiment

The purpose of this research was to further the V&V of MCNP6.1-generated NPF estimates by extending prior work that used a simplified vehicle surrogate shielded on all sides by 2.54 cm of steel [8]. New investigations reported here employed a surrogate vehicle shielded with basic ballistic armor more representative of that found on U.S. military vehicles. This new surrogate consisted of a box with side lengths of 62.27 cm and 3.175 cm thick walls, composed of material layers (from inside to out) of 1.27 cm steel, 1.27 cm glass reinforced plastic (GRP), and 0.635 cm aluminum, which represented the vehicle frame, anti-spallation liner, and skin, respectively. The ^{235}U fission neutron spectrum for this experiment was generated by the FBR located at WSMR.

Experimental Design

An armored vehicle surrogate was used, consistent with the legacy radiation transport experiments using similar surrogates constructed of iron or steel [2], [5]. The material plates were bolted to an internal frame, as depicted in Fig. 2, made of aluminum due its low microscopic cross section for fast and epithermal neutron absorption. The three-inch diameter hole at the top of Fig. 2 allowed for the insertion of the LiI(Eu) scintillator and photomultiplier tube into the polyethylene Bonner spheres, as required to measure the response of the shielded spectrometer within the armored vehicle surrogate. For unshielded measurements, the surrogate was simply removed.

In both experimental configurations, aluminum stability rings and an aluminum laboratory jack ensured consistent positioning and orientation of the scintillation crystal across all measurements. For every measurement, the LiI(Eu) scintillator was positioned at a horizontal distance of exactly 12 ft from the middle of the FBR and centered on it vertically.

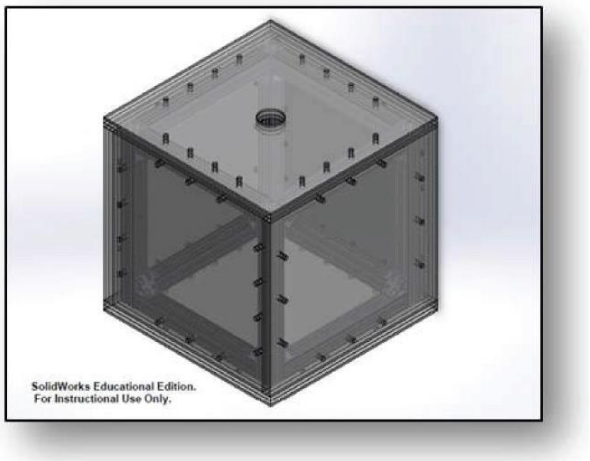

Figure 2. Schematic of the armored vehicle surrogate testing apparatus, shown with the scintillator opening in the upward position. The three armor layers are bolted to an aluminum frame during shielded measurements.

The absolute BSS count rates were recorded via Ortec Maestro software and associated uncertainties for both the shielded and unshielded configurations were input into the MAXED software, which unfolded the experimental solution spectra. Spectra were then normalized to facilitate comparison against the computational neutron flux spectra data.

Computational Design

The experimental geometry was replicated in MCNP6.1, including the armored vehicle surrogate. A depiction of the input file geometry is shown in Fig. 3 for the shielded configuration.

The FBR was modeled as a point source and incorporated a 235U fission energy spectra previously validated by FBR personnel. The source was collimated into a directional cone with a half-angle of 40° directed toward the armored vehicle surrogate. Shielded neutron flux was calculated using an F4 average neutron flux tally across the 12-in diameter sphere of air located in place of the largest Bonner sphere, as depicted in Fig. 3. The unshielded spectrum was simulated using the same tally and location in the absence of the vehicle surrogate. The MCNP6.1 computed neutron flux spectra for both configurations served as the a priori input into MAXED to assist in spectra deconvolution. Lastly, both the shielded and unshielded MCNP6.1 neutron spectra were normalized to experimental data to facilitate comparison.

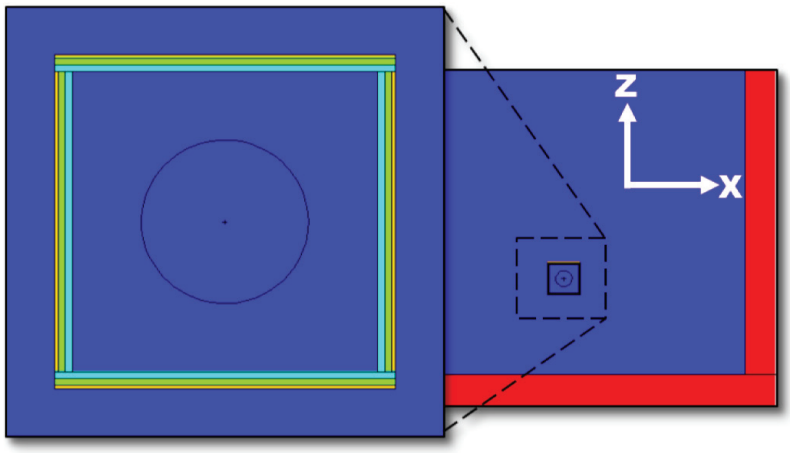

Figure 3. Horizontal view of the experiment geometry, as modeled in MCNP6.1. Dark blue represents air, while light blue is steel, green is GRP, orange is aluminum, and red is concrete.

Results and Analysis

Shielded Spectra Results

Fig. 4 shows the BSS-measured and MCNP6.1-simulated spectra within the armored vehicle surrogate when exposed to the ^{235}U neutron source generated by the FBR at WSMR. The spectra demonstrate reasonable structural and intensity agreement, especially above 100 keV and across the lower energies. As anticipated, the MAXED results suffered from low resolution inherent in the BSS across intermediate energies, which is likely responsible for the disparity in intensity across that energy region. The intensity disparity above 1.1 MeV is as yet unresolved, but appears systematic due to its consistent occurrence in past studies [8].

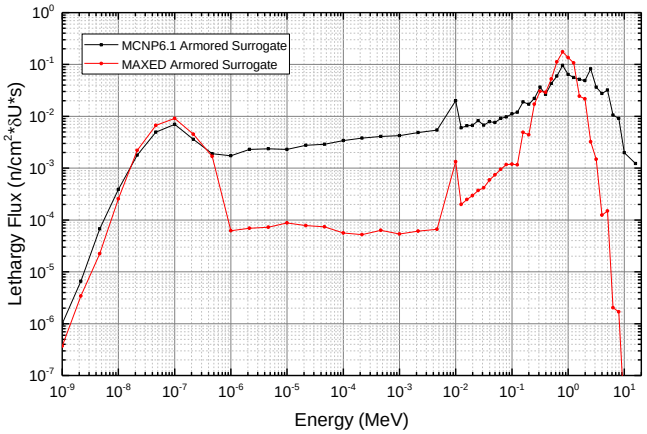

Fig. 4. Neutron spectra from the ^{235}U neutron source at the WSMR FBR as measured by a BSS within the armored vehicle surrogate (red) and computed by MCNP6.1 (black) in units of lethargy flux.

Despite these discrepancies, the neutron spectra share a similar shape and relative intensities anticipated for a ^{235}U fission source. The MAXED solution χ^2/df-value was 0.30, which indicated the solution spectrum matched the experimental data within the measurement error tolerances to a statistically significant degree. Based upon these factors, both spectra are deemed valid approximations for the spectral neutron flux present within the armored vehicle surrogate during exposure to the FBR.

Unshielded Spectra Results

Similarly, the unshielded neutron spectra demonstrate reasonable structural and intensity agreement, specifically across energy regions above 100 keV and at the lower energies. As shown in Fig. 5, the same BSS low-resolution effects are again present, as well as the expected peak in neutron lethargy flux for a ^{235}U fission source. Likewise, the same disparity in spectral intensity above 1.1 MeV can be observed.

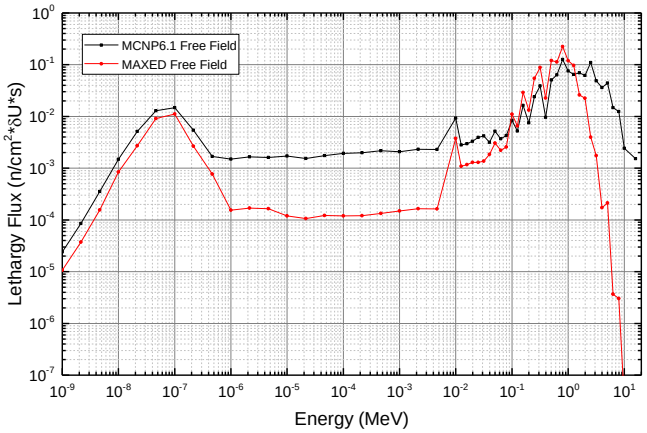

Fig. 5. Neutron spectra from the ^{235}U neutron source at the WSMR FBR as measured by a BSS in the unshielded configuration (red) and computed by MCNP6.1 (black) in units of lethargy flux.

The MAXED solution χ^2/df-value was 0.74, which indicated the solution spectrum matched the experimental data within the measurement error tolerances to a statistically significant degree. Based upon these factors, both free-field spectra are deemed valid approximations for the neutron flux present at a distance of 12 ft from the FBR.

5.1.1.8 Task 8

#	Material (S/C)	Geometry (S/C)	Source (Mono/Poly)	Spectra
8	C	S	Poly	Neutron

The following text, images, and data were presented as:
J.D. Glesmann, C.F. Smith, A.W. Decker, "Neutron Protection Factor Determination and Validation for a Vehicle Surrogate using a Californium Spontaneous Fission Source," oral presentation delivered at the 2018 Hardened Electronics and Radiation Technology Technical Interchange Meeting in Tucson, AZ on 19 April 2018.

Computational Approach (MCNP6)

To validate the measured NPFs in this research, MCNP6.1 simulations were developed for each of the experimental assemblies. The simulations included most, if not all, equipment in the RCL, the vehicle surrogate, and the source. The MCNP6.1 input file was provided by Dr. Luisa Hansen, who previously worked with Dr. Radoslav Radev to produce the RCL characterization report [5]. Modifications to Dr. Hansen's input file included the addition of the surrogate vehicle and fluence tallies with unique bin structures.

Figure 1 below shows the RCL facility as per Dr. Radev's report [5]. The room is 9.14 meters by 12.19 meters, with the N40 Irradiator system located slightly off center (at 4.48 meters by 6.29 meters). Prior experiments conducted by Dr. Radev were completed on the north side of the RCL facility at distances varying from 2 meters to 5 meters. The facility was large and was described as "minimal neutron backscatter" characteristics. The Cf-252 spontaneous fission source was seated with other sources in a concrete bunker approximately 11' beneath the aluminum flooring in the RCL. The MCNP6.1 simulation included the surrogate vehicle at approximately 3 meters from the source on the south side of the RCL facility.

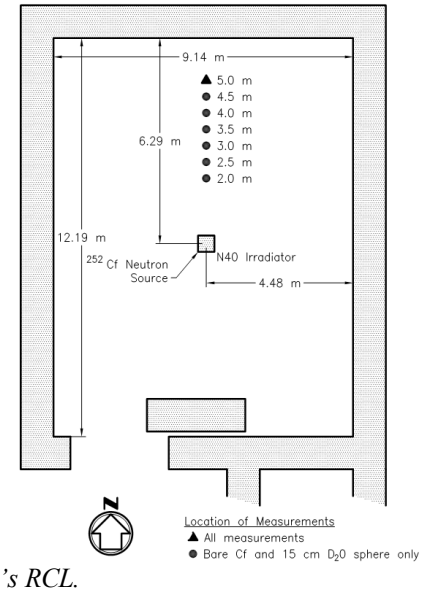

Fig. 1. Simple Schematic of LLNL's RCL.

The source was modeled in MCNP6.1 as an isotropic source characterized by the Watt Spontaneous Fission Spectrum [14] , with coefficients (a = 1.18 MeV and b=1.03419 1/MeV)

$$f(E) = C * exp\left(-\frac{E}{a}\right) * sinh(\sqrt{b * E}) \qquad (1)$$

Experimental Approach (BSS and Unfolding)

The experimental detection methodology chosen by DTRA to evaluate the flux within the surrogate vehicle was the Bonner Sphere Spectrometer (BSS) system [6]. The BSS consists of a ^{6}LiI(Eu) detector, six high-density polyethylene spheres, multiple ORTEC signal processing units, and the ORTEC Maestro data acquisition software. Figure 2 shows the 10" and 12" polyethylene spheres, along with the LiI(Eu) detector. Three additional spheres were used, but are not depicted in Figure 2.

Fig. 2. Bonner Sphere Polyethylene Spheres and LiI(Eu) Detector.

The RCL, vehicle surrogate, BSS system, and the N40 irradiator source transport system can be observed in Figure 3. The supporting equipment, such as the steel cart, plywood, and support wood under the vehicle surrogate were not accounted for in the simulated model. This could be a contribution to the difference or calculated error, described later.

Figure 3. Surrogate Vehicle Experimental Assembly

The experimental neutron fluence spectra were deconvoluted using the Unfolding with MAXED and GRAVEL, version 3.3, (UMG v3.3) unfolding software. Specifically, the Maximum Entropy Deconvolution algorithm in the UMG software package was used to converge on solution spectra for the given BSS measured data. Additionally, the integral quantities software (IQ), which uses a covariance matrix algorithm, was used to determine the error in the solution spectra from MAXED created during the unfolding process [7].

Experimental Results

Figure 4 shows the results of the unfolded spectra using UMG (MAXED) for both the surrogate vehicle and free field configurations. The results were plotted as a histogram of unmodified fluence per unit lethargy and upper energy bin values in mega-electron volts (MeV). The spectral characteristics of both the free field (FF) and surrogate vehicle (SV) are remarkably similar. The reduction in thermal and fast neutron fluence can be observed and follow similar trends to the iron-56, the primary component found in the steel in the surrogate vehicle, shielding characteristics. Additionally, to show the impact of the fluence to dose conversion coefficients, enumerated in the ICRP-74 [8] publication, a histogram (green) was overlaid on the unmodified fluence spectra. It is apparent that the reduction in thermal neutron fluence compared to the reduction in fast neutron fluence will be negligible after the ICRP's coefficients are applied and integrated.

The higher fluence observed with the surrogate vehicle in the epithermal neutron energies can be attributed to the dominating effects of the iron found in the steel plates. Iron-56 undergoes a nuclear resonance region from 10 KeV to 1 MeV for elastic, inelastic, and capture neutron interactions. In this epithermal neutron energy region, the likelihood for a neutron capture reaction to occur versus a scattering reaction is as much as six orders of magnitude, in barns, lower. In a region where scattering reactions significantly dominate, neutrons may become "trapped" inside of the surrogate vehicle, and could account for a NPF value of less than one for that specific discrete energy.

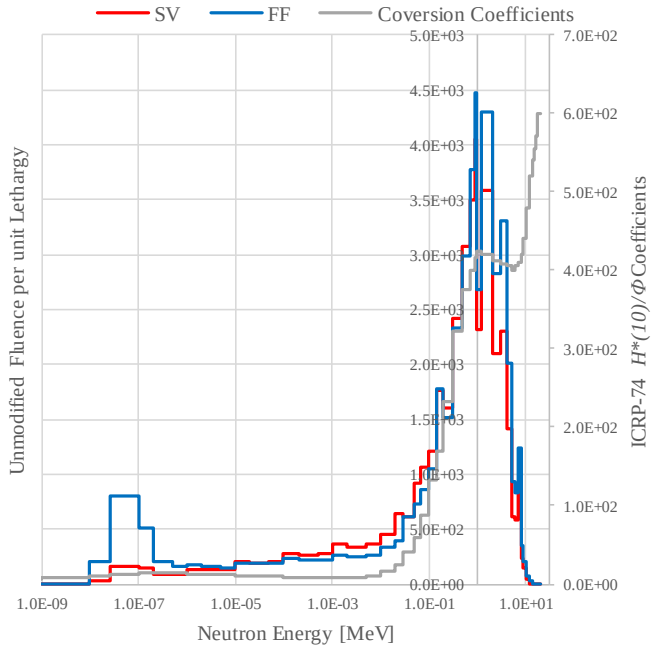

Fig. 4. Experimental Fluence Spectra.

Computational Results

Computational results were presented by three different methods for later comparison: a high resolution unmodified fluence tally, a high resolution modified fluence tally, and a low

resolution unmodified fluence tally. The high resolution tallies consisted of a 200 energy bin structure ranging from approximately 0 to 12.5 MeV, logarithmically spaced. The low resolution tally consisted of the same 47-bin energy bin structure found in the ICRP-74 fluence-to-dose conversion coefficients. However, the low resolution energy bin structure produced poor data in the experimental results as the a priori, or default spectrum. Therefore, only the higher resolution spectra were used for further calculations and comparison.

Later, it was discovered that after applying MCNP's standard dose function 1, the NPF values were greater than those resulting from manual application of the fluence-to-dose conversion coefficients. Because the experimental methodology applied the fluence-to-dose coefficients manually, the high resolution unmodified fluence tally was used. It is suspected that MCNP6.1 interpolates between the values found in the ICRP-74 publication to create the dose function, which could account for a higher NPF value. Instead, the unmodified fluence tally with 200 energy bins were summed and grouped to match the ICRP-74's 47-bin structure, which provided a means to easily apply the conversion coefficients.

In Figure 5, the results of the simulation are presented in a similar manner to Figure 4, but have already been converted to dose spectra and are normalized.

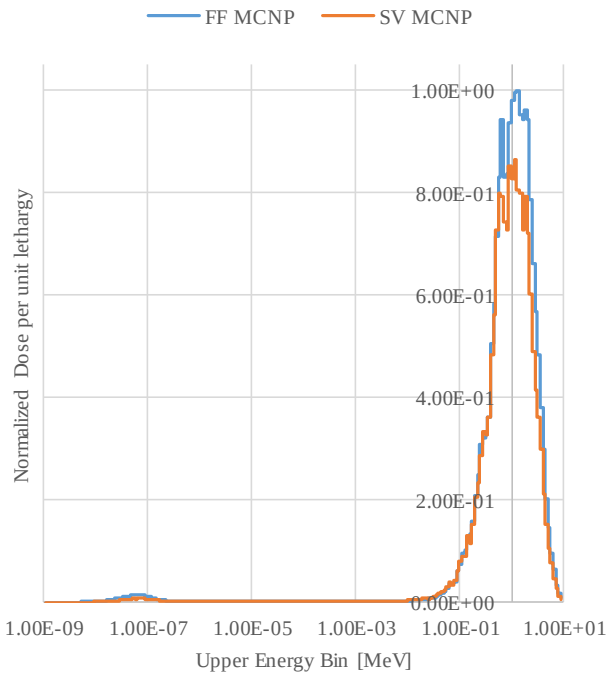

Fig. 5. Computational Dose Spectra

5.1.1.9 Task 9

#	Material (S/C)	Geometry (S/C)	Source (Mono/Poly)	Spectra
9	C	S	Poly	Gamma

The following text, images, and data were presented as:
D.W. Sundberg, J.A. Podpaly, J.C. Markulike, C.L. Bouvier, A.D. Decker, "Verification of MCNP6 Gamma Protection Factor Estimates for a Surrogate Armored Vehicle," poster presentation delivered at the 2017 Hardened Electronics and Radiation Technology Technical Interchange Meeting in Denver, CO on 27 April 2017.

Methodology

Experimental

The experiment utilized a 2ft× 2ft×2ft hollow armored vehicle surrogate with walls consisting of 0.25in aluminum, 0.5in GRP, and 0.5in steel, in the order shown in Figure 1. These materials represent a basic military ballistic armor, and previous research suggests this specific order provides the highest GPF value [4].

A 1 µCi 60Co source was utilized in this experiment due to its distinct poly-energetic gamma ray spectrum. The source was placed at an initial distance of 1 in and then moved further away in subsequent trials to a final distance of 12 in. Each trial lasted a total of 15 minutes, and the NaI(Tl) detector was placed inside the box to measure the gamma spectrum within the surrogate vehicle. Figure 1 provides an illustration of the experimental design for this research.

Fig. 1. The picture on the left shows the surrogate vehicle with layered materials (from outer to inner): 0.25in Aluminum, 0.5in GRP, and finally 0.5in steel. The picture shows the materials without the other shielded sides of the surrogate vehicle. The picture on the right depicts the experiment with a radioisotope placed a set distance from the surrogate vehicle.

A second experiment without the surrogate vehicle present determined the free-field gamma spectrum from the source at commensurate distances. The measured gamma spectra from both experiments were converted into units of dose equivalence, which facilitated GPF calculations for the physical experiment. Using Eq. 1, the free-field dose was divided by the shielded dose to calculate the experimental GPF of the surrogate vehicle.

Computational

MCNP6 was utilized to replicate the experimental geometry and environment described previously. Input decks created in MCNP6 and generated pulse height data that was used in an internal scaling function to convert it into dose, which will also use Eq. 1 to calculate GPF. These results were compared to the experimental results to provide a validation of the MCNP6 derived GPF estimates. The GPF for the steel layer was calculated, then the steel and GRP, finally the steel, GRP, and aluminum. This provided information about gamma attenuation of each layer. The factor to which each material contributed to the overall GPF was identified. An example of the geometry of the system produced by MCNPX Visual Editor can be seen in Fig. 2.

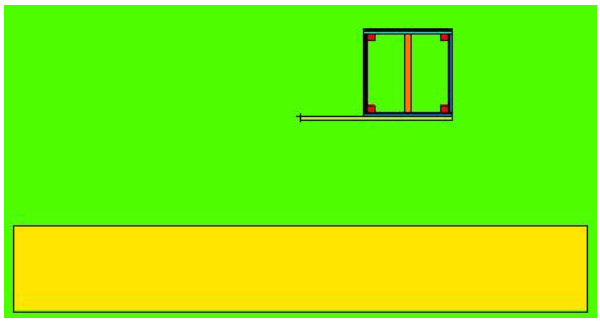

Fig. 2. Visual representation of the geometry of the experiment. In this cross section of the ZY plane, green represents air at room temperature and standard pressure, the red squares designate the aluminum frame for the surrogate vehicle, the yellow square represents the concrete floor in the room, the light green is the wooden table, the orange is the NaI(Tl) detector, and the blue layers are the three shielding materials.

Results

The results of this experiment are broken into two categories: Computational Results and Experimental Data. The computational data subsection contains the results from the MCNP6 c derived GPF calculations, while the experimental data subsection discusses results from the gamma ray spectra measured by the detector.

Computational Results

The dose was estimated using an F4 tally in MCNP, which provided the particle fluence of in units of (particles/cm2). The fluence was binned by predefined energy bins (MeV) and then multiplied by the activity of the source used in the experimental stage to create the flux per energy bin. Using MCNP6's internal dose function, the fluence was multiplied by internal photon flux-to-dose rate conversion factors to provide the dose rate (rem/hr). An example of this output is depicted in Fig. 3, which shows the dose rate of a 1 µCi ^{60}Co source incident on a fully shielded surrogate vehicle. The two full energy peaks of ^{60}Co can be seen at 1.173 and 1.332 MeV. These two peaks appear in 99% of all ^{60}Co decays and are often used as a source calibration tool. Additional trials utilized fewer energy bins to reduce computation time, and the difference in total bins had no significant effect on the overall GPF.

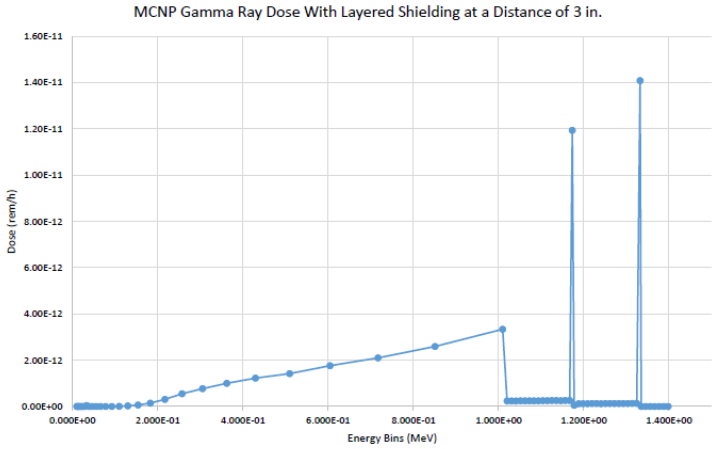

Fig. 3. MCNP output of dose from a ^{60}Co source tallied into different energy bins using all three layers of shielding and a simulated source distance of three inches.

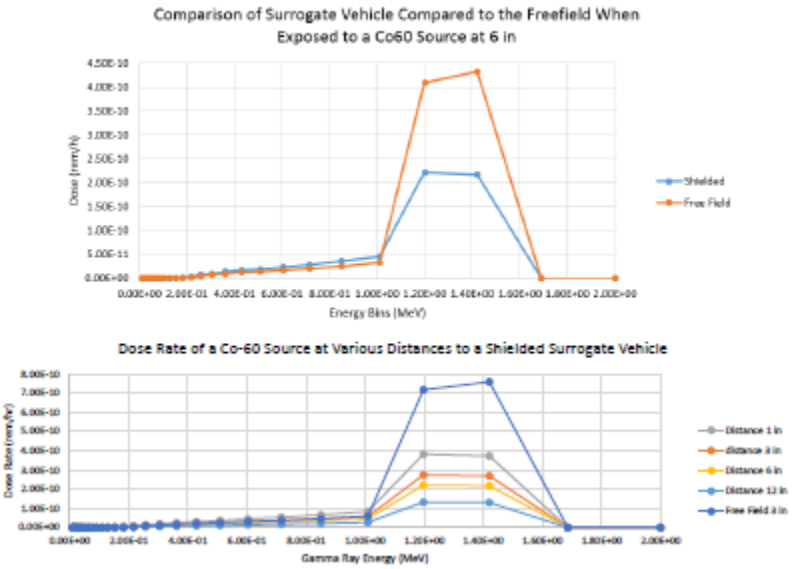

Fig. 4. MCNP output of dose from a ^{60}Co source tallied into different energy bins. The first graph shows the difference between the free-field dose when compared to the surrogate vehicle. The second graph plots dose at various distances between the ^{60}Co source and the surrogate vehicle.

Experimental Results

The experiment replicated the MCNP model. A 16”×4”×2” NaI(Tl) scintillator was used to capture the spectra from a 1µCi source, as depicted in Fig. 5. These spectra demonstrate agreement with the MCNP model in peak position.

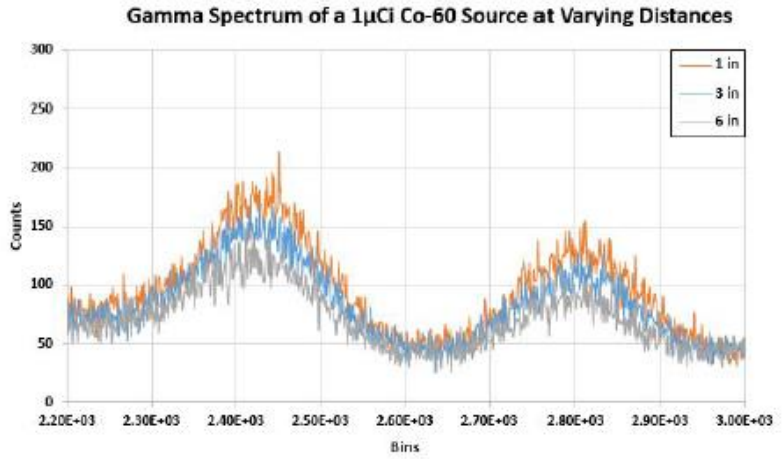

Fig. 5. Gamma ray spectra from a 1Ci source at distances ranging from one to six inches from the leading edge of the shielding. The two peaks represent the 1.173 and 1.332 MeV energy peaks from ^{60}Co source.

5.1.1.10 Task 10

#	Material (S/C)	Geometry (S/C)	Source (Mono/Poly)	Spectra
10	S	C	Poly	Neutron

The following text, images, and data were presented as:
A.W. Decker, S.A. Heider, S.R. McHale, M. Millett, J.W. McClory, J.A. Clinton, "Validation of MCNP6 Neutron Spectra Estimates Using Nested Steel Cubes at the WSMR FBR," oral presentation delivered at the 2017 IEEE Nuclear Science Symposium and Medical Imaging Conference in Atlanta, GA on 26 October 2017.

Experiment Design

The nested steel cubes measured 18in and 24in on their sides with walls 1in thick and were centered on the reactor core vertically at a horizontal distance of 12ft. The BSS and 4x4mm LiI(Eu) scintillator were centered within the innermost cube using an aluminum laboratory jack and stability rings.

Each cube wall consisted of two ½in steel plates, and steel screws affixed the plates to an interior aluminum frame. The experiment was replicated in MCNP6.1, as shown in Fig. 1. The model included half of the reactor room (walls, floor, and ceiling), the wood table, and the nested steel cubes. An F4 tally was used to estimate neutron flux within a 12in diameter sphere of air centered within the innermost cube.

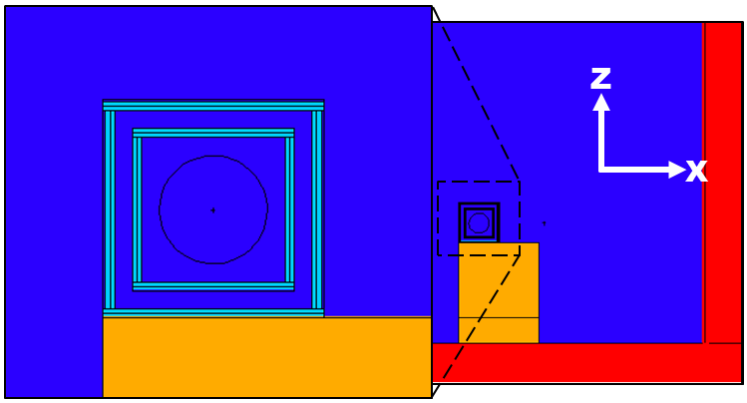

Figure 1. A visual representation of the geometry of the experiment modeled in MCNP6 and replicated in the physical experiment. The red represents the concrete walls of the FBR chamber, and the brown represents the wooden platform used to center the surrogate vertically on the FBR. Dark blue represents air, and the light blue is the steel of the nested cubes.

The free-field neutron spectrum was measured by identically positioning the BSS in 3D space. The BSS was supported by an aluminum laboratory jack, stability rings, and a 1¼in wooden spacer to account for the vertical height of the outermost cube. Removal of the steel cubes, the addition of the low-density spacer, and the presence of an aluminum lab clamp constituted the only changes between the free field and shielded experiment designs. Computationally, the MCNP6.1 free field model remained identical to that used for the shielded experiment, except for the removal of the steel cubes.

Free-field Spectra

As shown in Figure 2, the free-field spectra demonstrate good overall structural and intensity agreement throughout, and specifically across energies between 300 keV – 1 MeV. Systematic intensity disparities due to low resolution across the intermediate energy regions can be witnessed, as well as the expected peaks in neutron lethargy flux for a measured ^{235}U fission source. The χ^2–value for the MAXED solution was determined to be 0.97/df, which indicates the solution spectrum matches the experimental data to a statistically significant degree. Based upon these factors, both spectra are determined to be valid approximations for the neutron flux spectrum at that location within the free-field.

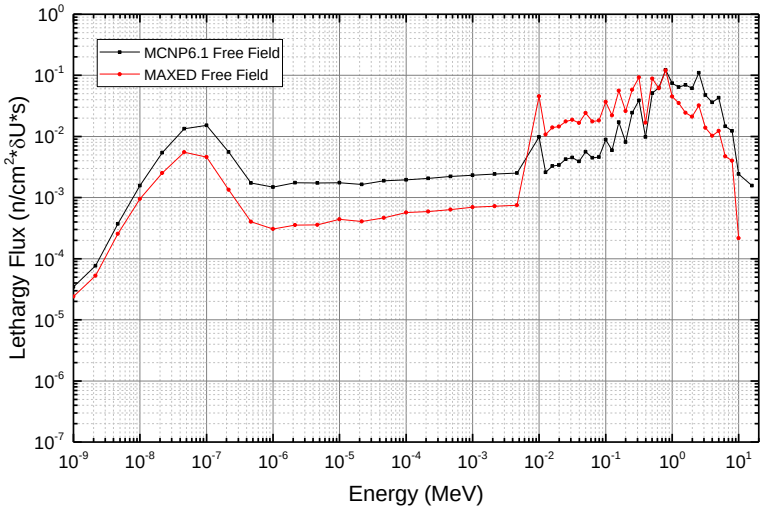

Figure 2. The free-field spectra comparison between MCNP6.1 and the MAXED deconvolution of the experimental BSS measurements.

Shielded Spectra

As shown in Fig. 3, the normalized shielded spectra demonstrate good overall structural and intensity agreement, especially below 50 eV. However, as anticipated, the MAXED results suffered from low resolution inherent in the BSS across the intermediate energy range, and the intensity disparity above 1 MeV is as yet unresolved. Despite the discrepancies, both neutron spectra reflect the overall shape expected from a ^{235}U fission neutron source. The reduced χ^2–value for the MAXED solution was determined to be 0.99/df, which indicates the solution spectrum matches the experimental data to a statistically significant degree. Based upon these factors, both spectra are determined to be valid assessments for the neutron flux within the nested cubes.

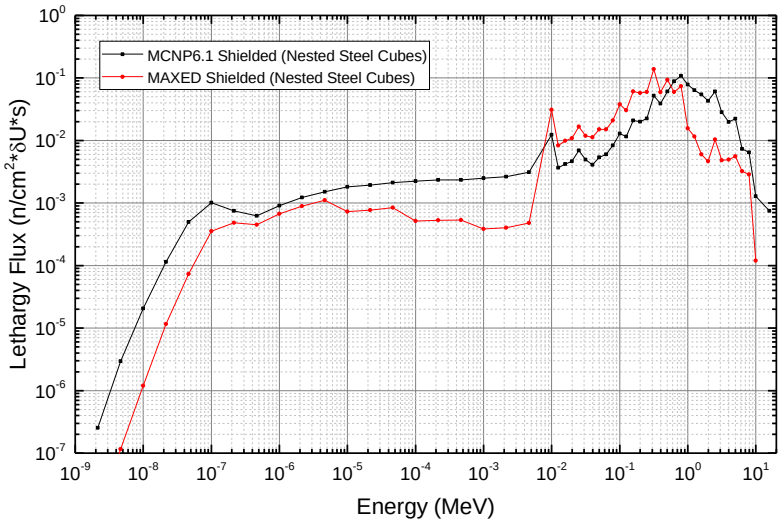

Figure 3. The shielded spectra comparison between MCNP6.1 and the MAXED deconvolution of the experimental BSS measurements.

5.1.1.11 Task 11

#	Material (S/C)	Geometry (S/C)	Source (Mono/Poly)	Spectra
12	S	C	Poly	Gamma

The following text, images, and data were presented as:
S.W. Callas, P.J. Gallucci, J.J. Veldkamp, A.W. Decker, "Validation of MCNP6.1 Gamma Protection Factor Estimates for a Nested Steel Cube Surrogate Vehicle," poster presentation at the 2018 American Nuclear Society Student Conference in Gainesville, FL on 06 April 2018.

Experiment:

This research utilized both experimental and computational methods in an effort to further validate MCNP6.1-derived GPF estimates for simplified military vehicles when exposed to a ^{137}Cs gamma spectrum, and this research builds upon a previous study conducted at West Point [7]. The surrogate vehicle was constructed using ½in thick rolled, homogenous steel plates bolted to aluminum framing. When fully assembled, the surrogate vehicle consisted of an outer 24in3 cube with steel walls ½in thick and a smaller, inner 18in3 cube with steel walls 1in thick. The nested cubes can be seen in Fig. 1 below.

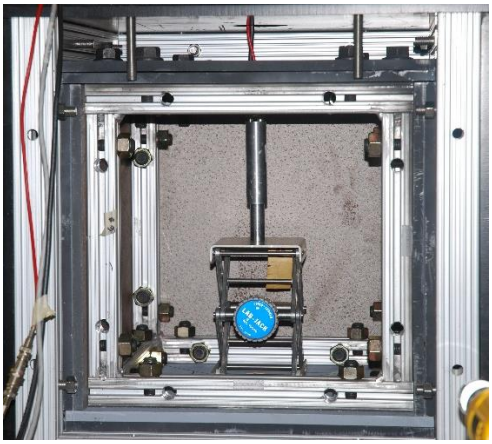

Fig. 1. Nested steel cubes constituting the surrogate military vehicle, which consisted of an outer 24in3 cube with steel walls ½in thick and a smaller, inner 18in3 cube with steel walls 1in thick. Both cubes were constructed using ½in steel plates bolted to inner aluminum frames. Of note, the detector shown in this image is not the 2in NaI used in this research; however, the positioning and set-up is consistent.

A 3in diameter hole centered through the top plates of both cubes allowed for the insertion a 2in NaI detector and photomultiplier tube, which was used to record the shielded gamma spectrum. The detector rested inside the inner cube on a 4×4in aluminum laboratory stand, which was adjusted in height to ensure the crystal was centered vertically within the enclosure. The detector cabling and top of the detector can be seen entering the surrogate in Fig. 2.

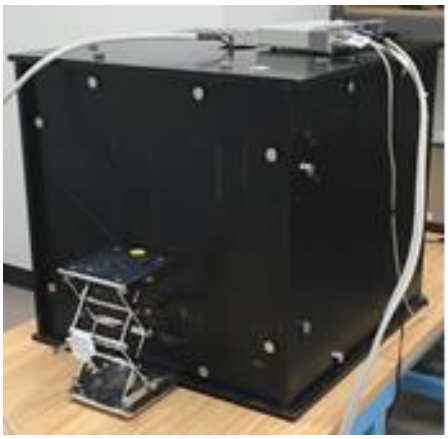

Fig. 2. NaI detector and cabling can be seen entering the surrogate vehicle through the 3in diameter hole located in the top of the outermost cube.

A separate aluminum laboratory stand was also used to position the ^{137}Cs source external to the surrogate vehicle, as shown in Fig. 2. The stand was adjusted to ensure the source was centered vertically and horizontally relative to the vehicle during all measurements, which put the source exactly 12in from the center of the detector crystal. Both source and detector position was consistent during shielded and unshielded measurements; however, for unshielded measurements the surrogate vehicle was removed from the table. The experimental measurements consisted of a 10min detector calibration followed by 24hrs of data collection for both the shielded and unshielded configurations, and all data was recorded using GammaVision software.

For the computational GPF assessment, MCNP6.1 was used to simulate the experimental environment, including both steel cubes encasing a 15cm spherical detector region filled with air. Fig. 3 is an XY-axis (top-down) image of the room in which the physical experiment occurred, with dark blue representing air, red representing concrete, and light blue representing the steel of the nested cubes. Omitted from this figure is the concrete floor and ceiling, as well as the detector volume and wooden table, which were also included in the model.

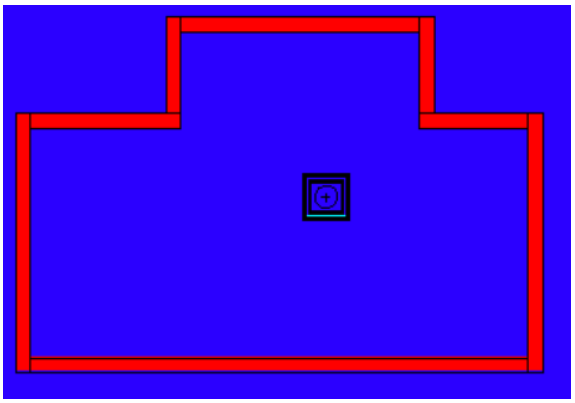

Figure 3. XY-axis (top-down) image of the room in which the physical experiment occurred, with dark blue representing air, red representing concrete, and light blue representing the steel of the nested cubes. Omitted from this figure is the concrete floor and ceiling, which were also included in the model.

The model used to compute the unshielded gamma flux was identical to the shielded simulation shown above; however, the surrogate vehicle was removed. The source was modeled as a point source in a location relative to surrogate vehicle consistent with that used in the physical experiment, and an F4 tally was used to estimate the photon flux energy spectra for both the shielded and unshielded configurations. In both simulations, sufficient particle tallies were recorded within the detector volume to reduce error <4% per energy bin.

Results and Discussion:

For the experimental measurements, the recorded spectra data were first normalized with an upper energy cutoff of 1 MeV. The recorded channels were then separated into bins, with each bin containing 4 channels. The counts for each bin were summed, and each channel was labeled with a percentage of bin contribution, which were used to create weighted energy averages for each bin. A graph of the experimental shielded and unshielded spectra are shown below in Fig. 4.

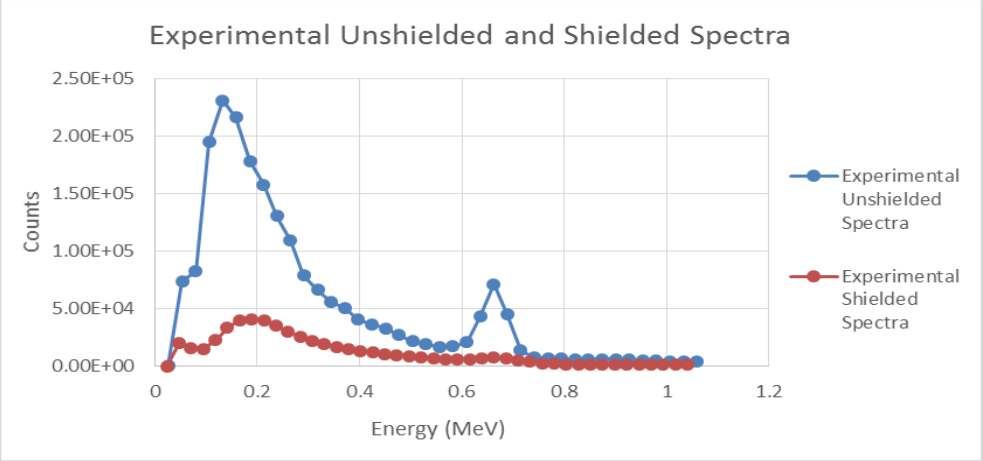

Fig. 4. Shown is the comparison between the spectra collected for the experimental shielded and unshielded trials, which reveals a marked decrease in count rates for the shielded configuration.

The process for normalizing and comparing the MCNP6.1-derived flux spectra for both the shielded and unshielded simulations was very similar, although MCNP6.1 allowed for the spectra to be produced automatically in the required energy bins. A plot of the shielded and unshielded MCNP6.1 spectra are shown below in Fig. 5.

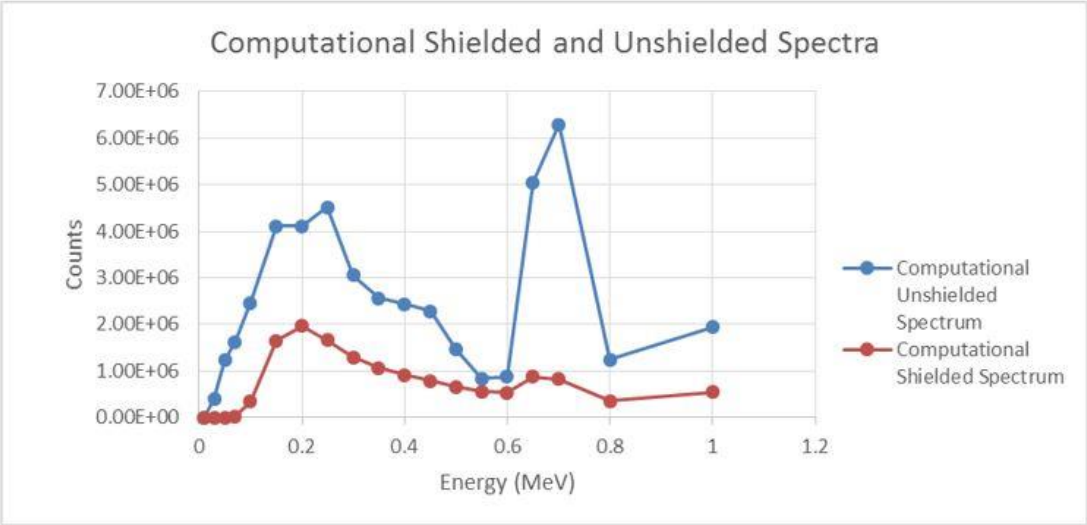

Fig. 5. Shown is the comparison between the spectra collected for the computational shielded and unshielded trials in MCNP6.1.

5.1.2. Data Validation Tasks Analysis

Definition of Validation:

1. The process of determining the degree to which a model and its associated data are an accurate representation of the real world from the perspective of the intended uses of the model.

2. The process of determining the fitness of a model or simulation and its associated data for a specific purpose.

For the purposes of this document, "validation" is achieved through the calculation and comparison of experimental and computational protection factors. If the disparity between these values is found to be <10%, including associated uncertainties, then the MCNP solution is found to be valid. This is essentially a comparison of the dose ratios between the free-field and shielded environments, as described in Eqs. 1-3. The matrix provided below in Table 3 provides the parameters for each task, and these investigations facilitate, in aggregate, the validation of MCNP6 for generating protection factor estimates.

Table 3: List of validation tasks for the RPF methodology, which focus on evaluations of MCNP6-derived RPF, NPF, and GPF values when compared to those calculated from experimental measurements. Again, the task matrix utilized a deliberate and sequential combination of simple (S) and complex (C) materials and geometry, as well as source spectra.

Validation Tasks				
#	Material (S/C)	Geometry (S/C)	Source (Mono/Poly)	Protection Factor
1	S	S	Mono	NPF
2	S	S	Mono	GPF
3	**S**	**S**	**Poly**	**NPF**
4	C	S	Mono	NPF
5	C	S	Mono	GPF

6	C	S	Poly	RPF
7	**C**	**S**	**Poly**	**NPF**
8	C	S	Poly	NPF
9	C	S	Poly	GPF
10	**S**	**C**	**Poly**	**NPF**
11	S	C	Mono	GPF

The research findings for each individual task are included below, along with a listed citation for the conclusions presented.

5.1.2.1 Task 1

#	Material (S/C)	Geometry (S/C)	Source (Mono/Poly)	Protection Factor
1	S	S	Mono	NPF

The following text, images, and data were published as:
A.W. Decker, M.P. Shannon, J.A. Clinton, J.W. McClory, S.R. McHale, "Verification and Validation of Monte Carlo N-particle Code 6 (MCNP6) with Neutron Protection Factor Measurements of an Iron Box", *Journal of Radiation Effects, Research and Engineering*, vol. 33, no. 1-E, pp. 252-259, May 2015.

Results and Discussion

Whereas our earlier approximation of NPF via equation (1) in Section 2.1 did not incorporate ICRP-published neutron flux-to-dose equivalent rate conversion factors, here we report an accurate NPF, using H(10) values from both MCNP6-computed box and free-field spectra as well as flux-to-dose conversion coefficients published by Veinot and Hertel (2005) [13], which incorporate the most recent guidance provided by the ICRP Publication 60 and the ICRU Report 49. Although the propagation of error is straightforward, the uncertainties associated with the MAXED software could not be determined readily. Consequently, the uncertainty for each MAXED solution spectrum was estimated at 10%, which is conservative based upon previously reported error estimates of radiation protection factors [4, 14, 15]. Using this methodology and equation (1), the experimentally-measured NPF, using BSS and MAXED unfolding was calculated as 1.27 ± 0.18, and the MCNP6-computed NPF was 1.26 ± 0.28. These observed NPFs, and the fact that NPF calculations are based on statistically significant MAXED-generated flux spectra, implies that the MCNP6-derived NPF assessment may be considered significantly close to the true NPF value. Thus, in future research we can confidently apply MCNP6 for neutron protection factor assessments of military vehicles that are exposed to mono-energetic neutron sources.*

5.1.2.2 Task 2

#	Material (S/C)	Geometry (S/C)	Source (Mono/Poly)	Protection Factor
2	S	S	Mono	GPF

The following text, images, and data were presented as:
W. Erwin, J. Clinton, J. McClory, B. Singleton, "Verification and Validation of Monte-Carlo N-Particle 6 (MCNP6) for Computing Gamma Protection Factors," poster presentation delivered at the 2015 Hardened Electronics and Radiation Technology Technical Interchange Meeting in Chantilly, VA on 23 April 2015.

Results and Discussion:

For the initial validation experiment, the experimental GPF was 3.3% more than the model GPF, and the 95% confidence interval of the MCNP6 model's GPF was bounded within 5% of the experimental result. Therefore, the model passed validation.

Source	*MCNP6 GPF*	*Experimental GPF*	*% Disparity*
^{137}Cs	*2.16*	*2.12*	*1.89*
^{60}Co	*1.76*	*1.83*	*3.83*

Alternate configurations of the initial experiment yielded mixed results. The higher energy photons from ^{137}Cs and ^{60}Co sources produced valid results, while weaker sources did not, due to limitations of the NaI detector system at lower energies. Placing sources at the edge and corners of the enclosure posed some challenges for the model, as this placed a light aluminum frame in the direct path of the photons. The presence of the aluminum, though far lighter than the steel, raised the experimental GPF by 5-8%. Additionally, the GPFs computed at the edges and corners was somewhat higher than expected, consistent with an analytical model of a slab with a width equal to the diagonal distance across the steel corners and edges.

5.1.2.3 Task 3

#	Material (S/C)	Geometry (S/C)	Source (Mono/Poly)	Protection Factor
3	S	S	Poly	NPF

The following text, images, and data were published as:
A.W. Decker, S.R. McHale, J.A. Clinton, J.W. McClory, M. Millett, "Verification and Validation of MCNP6.1 Neutron Protection Factor Estimates Using the WSMR Fast Burst Reactor," *Journal of Radiation Effects, Research and Engineering*, vol. 35, no.1, pp. 52-58, Apr. 2017.

NPF Calculation

Calculations of ambient dose equivalence (H(10)) utilized neutron flux-to-dose conversion coefficients published by Veinot and Hertel [14]. Using these values, solution spectra from both MCNP6.1 and MAXED were converted to total values of total H*(10). Uncertainty propagation for MCNP6.1-derived spectra occurred in a straightforward manner; increasing particle tallies minimized variance and associated error. MCNP6.1 solutions passed all ten statistical checks typically performed by MCNP to gauge tally behavior. Traditional error propagation for the experimentally measured spectra could not occur due to a lack of associated uncertainties from MAXED. Consequently, uncertainty for the MAXED solution spectra was estimated at 5% and propagated forward, which is conservative based on previous research [5].*

Based upon calculated H(10) values, the NPF estimate provided by MCNP6.1 differed from the experimentally-derived NPF by ~5% relative error, as shown below in Table I.*

Table I. Experimental and computational NPF values.

Method	*NPF ± ε*
Experimental (BSS and MAXED)	*1.14 ± .08*
Computational (MCNP6.1)	*1.08 ± .02*

This result is statistically significant based upon the degree of agreement and small relative uncertainties when compared to previously reported error estimates for RPFs [2-4]. This strongly supports further research into the V&V of MCNP6.1 for RPF assessments of military vehicles.

5.1.2.4 Task 4

#	Material (S/C)	Geometry (S/C)	Source (Mono/Poly)	Protection Factor
4	C	S	Mono	NPF

The following text, images, and data were submitted for publication as:
J.D. Glesmann, M.G. Millett, M.E. Nelson, "Measurement and Model Validation of Neutron Protection Factors with a D-T Neutron Generator," Submitted to the Journal of Radiation Effects, Research and Engineering, vol. 35, 2017.

Conclusions

Table I summarizes the determined NPFs for the computational and experimental methods. While criteria for code validation have not yet been established, these values are deemed to be in relatively good agreement. The 6% difference seen between both NPFs was not unexpected, as both the fidelity of the model and fidelity of the unfolding are likely to have introduced some error.

Table I. NPF values for experimental and computational methods.

Configuration	*NPF*
Experimental	*1.09*
Computational	*1.03*

It has been shown that for simple geometries and shield compositions, the use of MCNP6 may provide a reasonable means for computationally determining NPFs. It may be possible, then, to determine NPF values against weapon radiation environments for actual vehicles and shielding configurations through MCNP simulations.

5.1.2.5 Task 5

#	Material (S/C)	Geometry (S/C)	Source (Mono/Poly)	Protection Factor
5	C	S	Mono	GPF

The following text, images, and data were published as:
T.J. Gates, C.R. Zeigler, C. Bouvier, A.W. Decker, "Verification and Validation of MCNP6.1 for Gamma Protection Factor Estimates of an Armored Box," *Journal of Radiation Effects, Research and Engineering*, vol. 35, no.1, pp. 76-82, Apr. 2017.

Experimental Analysis

The higher number of counts and the increased dose rate present in the lower energy region of the unshielded data was likely due to down-scattering of higher energy photons from interactions with the shield material layers. However, at higher energy regions around 662 keV, significantly lowering count rates are reported due to the shielding attenuation. Therefore, the data presented is Fig. 7 is logical, and data analysis resulted in a measured GPF value of 1.46 ± 0.01 for the armored box.

Computational Analysis

The computationally-derived data provided similar graphs of spectra when plotted. Fig. 8 shows both the normalized F6 Tally (counts) and F8 Tally (dose rate). These graphs were enhanced to reveal spectra disparity at lower energy regions, which produces a similar trend in data to those measured experimentally. These data resulted in a MCNP6.1-derived GPF estimate of 1.53 ± 0.01 for the armored box in the basic configuration.

Based upon this data, the experimentally measured and MCNP6.1-derived GPF values differ by just 4.6%. This result supports the further V&V of MCNP6.1 for GPF and RPF estimates of military vehicles.

5.1.2.6 Task 6

#	Material (S/C)	Geometry (S/C)	Source (Mono/Poly)	Protection Factor
6	C	S	Poly	RPF

The following text, images, and data were published as:
W.J. Erwin, E. Cazalas, J.W. McClory, A.W. Decker, "Development of Radiation Protection Factors with Gamma and Neutron Spectroscopy using a Plutonium-Beryllium Source," *Journal of Radiation Effects, Research and Engineering*, vol. 36, no.1, pp. 88-94, Apr. 2018.

Gamma Protection Factor Analysis

Fig. 3 displays the experimental and MCNP6-derived GPF results. The extended plotting of GPF_{Exp} at energies greater than ~5 MeV represents pulse pileup in experiment. Fig. 3 shows that while MCNP6 code did not include pulse pileup, GPF_{MCNP} matches GPF_{Exp} for energies up to 4.5 MeV. High energy contributions are still accounted for by the higher Compton continuums in the 4 MeV region in simulation, as would be observed in a detector absent of pulse pileup. The large error bars of observations taken above these energies are caused by low detection rates in this region. These low detection rates also mitigate the contributions of these higher energy bins to overall dose calculations and the associated experimental uncertainty. GPF results displayed in Fig. 3 are derived from the ratio of dose rates summed over the entire spectra, $\dot{D}_{FF}/\dot{D}_{SH}$.. Fig. 3 exhibits the importance of shielding against higher

energy gammas (4.43 MeV) and the potential for producing lower energy Compton scattered photons (< ~1 MeV) due to shielding.

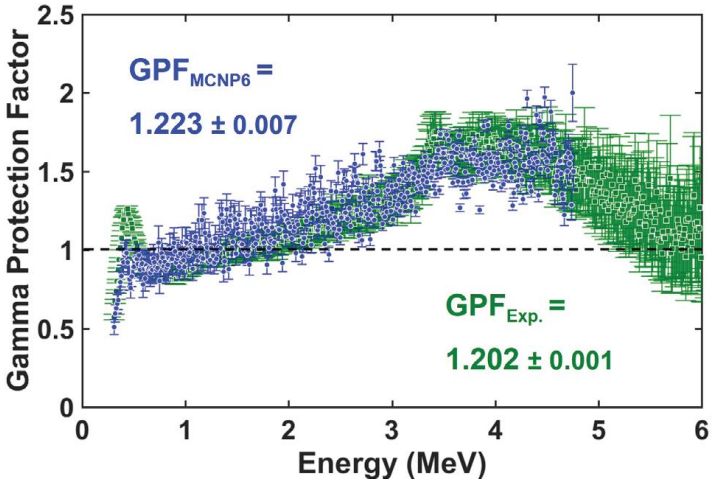

Figure 3. The overlaid gamma protection factor (GPF) results from MCNP simulation (GPF_{MCNP} in blue) and experiment ($GPF_{Exp.}$ in green) show good agreement up to 4.5 MeV. Error bars indicate standard error by bin. These standard error bars are calculated as the standard deviation of the photon energy deposited in each bin normalized to the energy of that bin. Standard deviations of the $GPF_{Exp.}$ at higher energies are larger due to low count rates of pulse pileup events. Above and below the dotted line, at GPF = 1, the shielding either reduces or increases the dose in the detector depending on the energy of the detected photons.

Neutron Protection Factor Results

Studies into the comparison of experimental and MCNP6 simulated setups have shown close agreement between NPF_{MCNP6} and $NPF_{Exp.}$[7], [8], [14]. Here, the NPF value is derived from an MCNP6 simulation using the experimental setup in Fig. 1. Dose is calculated by extracting results from an F4:n flux tally. Dose is derived from a log-log interpolation of neutron flux-to-dose conversion tables provided in ICRP 74 [15]. Dose results, displayed in Fig. 4, show that dose is imparted by both neutron absorption (at lower energies) and scattering (at higher energies). Fig. 4 also shows that the shield had mediocre qualities for neutron dose reduction as exhibited in the NPF_{MCNP6}, which is qualitatively expected given the thickness and material makeup of the shield. Interestingly, the dose with shield is increased at lower energies (< ~1 MeV) due to neutron down-scattering and subsequent absorption. However, the larger flux of higher energy neutrons dominates the neutron protection factor as $NPF_{MCNP6} > 1$.

Combined Radiation Protection Factor

The combined RPF value is an important metric of the dose reduction provided by a given shield in mixed gamma/neutron radiation fields. In this work, the RPF value is calculated from dose rates derived from the MCNP6 simulation of the experimental arrangement in Fig. 1. The combined RPF is calculated using Equation 2 and results in an RPF = 1.187 ± 0.003. While it appears that the RPF value can be alternatively calculated by averaging the NPF and GPF values, this will only yield the correct RPF value if shielded neutron and gamma doses are the same or when the GPF and NPF values are the same.

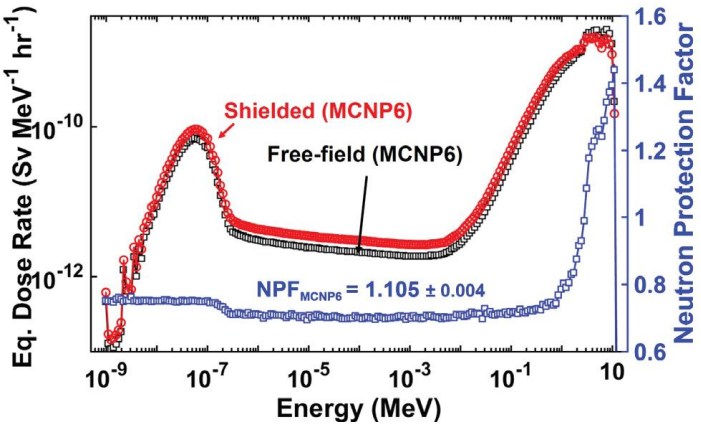

Figure 4. The neutron equivalent dose for free-field and shielded cases derived from the MCNP6 simulation of the experimental setup in Fig. 1. The neutron protection factor (right axis) shows that presence of the shield actually increases dose for energies lower than ~1 MeV. Standard errors are included for all data but are smaller than the data points displayed.

5.1.2.7 Task 7

#	Material (S/C)	Geometry (S/C)	Source (Mono/Poly)	Protection Factor
7	C	S	Poly	NPF

The following text, images, and data were published as:
A.W. Decker, S.A. Heider, S.R. McHale, J.A. Clinton, J.W. McClory, M. Millett, "Verification and Validation of MCNP6.1 Neutron Protection Factor Estimates of an Armored Vehicle Surrogate Using the WSMR Fast Burst Reactor," *Journal of Radiation Effects, Research and Engineering*, vol. 36, no.1, pp. 65-71, Apr. 2018.

NPF Calculation

Calculations of ambient neutron dose equivalent (H(10)) utilized neutron flux-to-dose conversion coefficients published by Veinot and Hertel [17]. Using these values, solution spectra from both MCNP6.1 and MAXED were converted to total values of H*(10).*

For the MCNP6.1-derived neutron spectra, uncertainty propagation occurred in a straightforward manner; increasing particle tallies minimized variance and associated error. MCNP6.1 solutions passed all ten statistical checks typically performed by MCNP to gauge tally behavior. Traditional error propagation for the experimentally measured spectra could not occur due to a lack of associated uncertainties from MAXED. Consequently, uncertainty for the MAXED solution spectra was estimated at 5% and propagated forward, which is conservative based on previous research [5, 8].

Based upon calculated H(10) values, the NPF estimate provided by MCNP6.1 differed from the experimentally-derived value by ~4% relative error, as shown below in Table I.*

Table I. Experimental and computational NPF values.

Method	*NPF ± ε*
Experimental (BSS and MAXED)	*1.22 ± 0.06*
Computational (MCNP6.1)	*1.18 ± 0.02*

This result is statistically significant based upon the degree of agreement and small relative uncertainties when compared to previously reported error estimates for RPFs [2-4]. Additionally, when compared to similar NPF research using steel shielding alone, these results indicate the new surrogate armor materials offer improved protection against neutrons [8]. These findings strongly supports further research into the V&V of MCNP6.1 for RPF assessments of military vehicles.

5.1.2.8 Task 8

#	Material (S/C)	Geometry (S/C)	Source (Mono/Poly)	Protection Factor
8	C	S	Poly	NPF

The following text, images, and data were presented as:
J.D. Glesmann, C.F. Smith, A.D. Decker, "Neutron Protection Factor Determination and Validation for a Vehicle Surrogate using a Californium Spontaneous Fission Source," oral presentation delivered at the 2018 Hardened Electronics and Radiation Technology Technical Interchange Meeting in Tucson, AZ on 19 April 2018.

Results and Discussion

The final experimental NPF determined was 1.16 with an error bound of approximately +/- 0.05. Error determination and methodology is explained later in this paper. Upon integrating the dose spectra in Figure 5, the MCNP results produced a NPF of 1.1601, approximately 0.36% difference from the experimental NPF value. The error bound for the simulated NPF was approximately +/- 0.004, and was reported by MCNP.

Error Analysis

Two separate error analyses were done on the presented data using MCNP6.1's reported variance values and UMG's Integral Quantities (IQ) software included in the unfolding software package. The IQ software evaluates the solution spectrum's "sensitivity," or combined error through the use of the covariance matrix form. The sources of error the IQ considers are statistical in both the experimental data and the a priori. Table 1 presents the error from all known sources, other than operator induced error, and the respective IQ output error.

Table I. Experimental NPF value with reported error sources and error bounds.

Unfolded Error		
	Free-field	*Surrogate Vehicle*
Measured Data Error	*1.28E+00*	*1.40E+00*

A Priori Error	*3.30E+00*	*3.57E+00*
Combined	*3.60E+00*	*3.89E+00*
σ^2	*1.30E-03*	*1.51E-03*
$\Sigma\sigma^2$	*2.81E-03*	
Sqrt. Sum	*0.053044396*	
NPF	*1.1559E+00*	
+	*1.2090E+00*	
-	*1.1029E+00*	

The values "+" and "-" represent the NPF with the applied error bounds, upper and lower bounds respectively. Because it was found that the error introduced by the a priori, or theoretical guess from the MCNP6.1 output, was the dominating error, an additional effort was made for error reduction.

The statistical error in MCNP is driven by the number of particles stipulated by the user in the modeled problem. The above error calculations and data presented before were completed for 1.5E+07 neutrons in the MCNP6.1 simulation. In an effort to see the total effect of the a priori error, this value was changed to approximately 8.0E+07. The results are presented below in Table II.

Table II. Experimental NPF value with reported reduced error sources and error bounds.

Reduced Unfolded Error		
	Free-field	*Surrogate Vehicle*
Measured Data Error	*1.28E+00*	*1.40E+00*
A Priori Error	*1.43E+00*	*1.55E+00*
Combined	*2.00E+00*	*2.16E+00*
σ^2	*3.99E-04*	*4.65E-04*
$\Sigma\sigma^2$	*8.65E-04*	
Sqrt. Sum	*0.029402609*	
NPF	*1.1559E+00*	
+	*1.1853E+00*	
-	*1.1265E+00*	
a priori NPS value:	*7.957E+07*	

The total error was reduced to approximately half, by increasing the number of particles. If additional computational resources were immediately available, it is expected that this error introduced by the a priori estimate could have been reduced even further.

5.1.2.9 Task 9

#	Material (S/C)	Geometry (S/C)	Source (Mono/Poly)	Protection Factor
9	C	S	Poly	GPF

The following text, images, and data were presented as:
D.W. Sundberg, J.A. Podpaly, J.C. Markulike, C.L. Bouvier, A.D. Decker, "Verification of MCNP6 Gamma Protection Factor Estimates for a Surrogate Armored Vehicle," poster presentation delivered at the 2017 Hardened Electronics and Radiation Technology Technical Interchange Meeting in Denver, CO on 27 April 2017.

Computational Results

When the distance between the source and the surrogate vehicle was increased, the overall dose imparted on the surrogate vehicle was reduced, which was expected. The total GPF remained consistent despite the change in distance. Fig. 4 shows that as the distance increases, the dose rate decreases, which means fewer gamma rays interacted with the detector. This effect can be seen in comparing both Fig. 4 and Table I.

Table I. GPF Contribution Analysis by Material

	1"	3"	6"
Steel	1.34 ± 0.01	1.34 ± 0.01	1.34 ± 0.01
GRP	0.103 ± 0.004	0.103 ± 0.002	0.103 ± 0.002
Aluminum	0.086 ± 0.005	0.088 ± 0.003	0.086 ± 0.002
Total	1.52 ± 0.01	1.53 ± 0.01	1.53 ± 0.01

Despite changing the distances, each material maintained its contributions to the total GPF value. Each simulation at a different distance maintained the ratio between the free field and the shielded doses. As Table I shows, in every trial the steel contributed most to the overall GPF of the system, which was due to its higher atomic number, compared to either the GRP or aluminum [5]. The doses provided by MCNP passed all statistical checks and was within 6% difference at its largest difference which shows good fidelity in the data.

Experimental Results

From Table II we can see that as the source moves further away from our surrogate vehicle the GPF value becomes more similar to our computation results. This falls in line with what we expected as the source has some slight geometric differences from what MCNP modeled as a point source. As the distance increases the source more closely models a perfect point source. The difference between our experimental and computational results range from 6% at 1" to 0.65% at 6".

Table II. Experimental Dose and GPF

Trial	Shielded Dose ($\frac{mrem}{hr}$)	GPF
1"	$1.57 \times 10^{-7} \pm 0.003$	1.45 ± 0.002
3"	$1.07 \times 10^{-7} \pm 0.002$	1.51 ± 0.002
6"	$6.14 \times 10^{-8} \pm 0.003$	1.54 ± 0.002

GPF Assessment

The computational and experimental GPF values show good agreement. The largest difference between the MCNP and the experimental results occurs at 1", with a difference in value of 6%. This is due to possible saturation of the detector resulting from the closer proximity to the source. For the other trials, particularly at 6", is below 1%. These results increase confidence in the ability of MCNP6 to estimate GPFs for military vehicles.

Table III. GPF Comparison

Trial	MCNP GPF	Experiment GPF
1"	1.52 ± 0.002	1.45 ± 0.002
3"	1.53 ± 0.003	1.51 ± 0.002
6"	1.53 ± 0.003	1.54 ± 0.002

5.1.2.10 Task 10

#	Material (S/C)	Geometry (S/C)	Source (Mono/Poly)	Protection Factor
10	S	C	Poly	NPF

The following text, images, and data were presented as:
A.W. Decker, S.A. Heider, S.R. McHale, M. Millett, J.W. McClory, J.A. Clinton, "Validation of MCNP6 Neutron Spectra Estimates Using Nested Steel Cubes at the WSMR FBR," oral presentation delivered at the 2017 IEEE Nuclear Science Symposium and Medical Imaging Conference in Atlanta, GA on 26 October 2017.

Results and Discussion

Calculations of Ambient Dose Equivalence (H(10)) utilized neutron flux-to-dose conversion coefficients published by Veinot and Hertel (2005). These were applied to both the MCNP6.1 and MAXED spectra, and total doses were calculated. For MCNP6.1-derived spectra, uncertainty propagation was straightforward across all energy bins. Spectra were refined using a greater number of particle tallies to reduce variance, and the MCNP6.1 spectra passed all ten statistical checks typically performed to gauge tally behavior. Due to the lack of associated uncertainties from MAXED solutions, traditional error propagation could not occur. Consequently, uncertainty for the MAXED solution spectra was conservatively estimated as 5%.*

Based upon the computed values for H(10), the dose ratio assessment for the nested steel cubes provided by MCNP6.1 differed from the experimentally-derived dose ratio by <5% relative error, as shown below in Table I.*

Table I. NPF Analysis

Method	*NPF* $\pm \varepsilon$
Experimental (BSS and MAXED)	1.184 ± 0.085
Computational (MCNP6.1)	1.143 ± 0.014

This represents a statistically significant result, which supports further research into the validation of MCNP6 for NPF assessments.

5.1.2.11 Task 11

#	Material (S/C)	Geometry (S/C)	Source (Mono/Poly)	Protection Factor
12	S	C	Poly	GPF

The following text, images, and data were presented as:
S.W. Callas, P.J. Gallucci, J.J. Veldkamp, A.W. Decker, "Validation of MCNP6.1 Gamma Protection Factor Estimates for a Nested Steel Cube Surrogate Vehicle," poster presentation at the 2018 American Nuclear Society Student Conference in Gainesville, FL on 06 April 2018.

Results and Discussion

For both sets of spectra, fluence-to-dose conversion factors were applied to each bin and summed across all energies for both the shielded and unshielded spectra to calculate total values of effective dose rate in units of rem/hr [6]. Using Eq. 2, experimental and computational GPF values were calculated from the ratios of those total effective dose values.

Table 1. Results of both the experimentally measured and computationally estimated GPF for the surrogate military vehicle used in these experiments.

Trial	GFP	δ
Computational Model	3.59	0.005
Experimental Model	3.64	0.08

The GPF values for the two models are within 3% of each other, demonstrating a high degree of accuracy between MCNP6.1 and the experimental, real-world design. The remaining error could likely be reduced with further increases in fidelity between the computational model and the experimental model, such as modeling the NaI detector crystal and applying its response function to the computed spectra.

5.2. Results Verification Task Analysis

Based on the results detailed in sections 5.1.1, all verification tasks are considered satisfactorily complete and address all M&S Requirements and Acceptability Criteria detailed in section 3 of this report.

Verification Tasks					Complete?
#	Material (S/C)	Geometry (S/C)	Source (Mono/Poly)	Spectra	(Y/N)
1	S	S	Mono	Neutron	Y
2	S	S	Mono	Gamma	Y
3	**S**	**S**	**Poly**	**Neutron**	Y
4	C	S	Mono	Neutron	Y
5	C	S	Mono	Gamma	Y
6	C	S	Poly	Gamma + Neutron	Y

7	**C**	**S**	**Poly**	**Neutron**	Y
8	C	S	Poly	Neutron	Y
9	C	S	Poly	Gamma	Y
10	**S**	**C**	**Poly**	**Neutron**	Y
11	S	C	Poly	Gamma	Y

5.3. Results Validation Task Analysis

Based on the results detailed in sections 5.1.2., all validation tasks are considered satisfactorily complete and address all M&S Requirements and Acceptability Criteria detailed in section 3 of this report.

Validation Tasks				Complete?
Material (S/C)	Geometry (S/C)	Source (Mono/Poly)	Protection Factor	(Y/N)
S	S	Mono	NPF	Y
S	S	Mono	GPF	Y
S	**S**	**Poly**	**NPF**	Y
C	S	Mono	NPF	Y
C	S	Mono	GPF	Y
C	S	Poly	RPF	Y
C	**S**	**Poly**	**NPF**	Y
C	S	Poly	NPF	Y
C	S	Poly	GPF	Y
S	**C**	**Poly**	**NPF**	Y
S	C	Mono	GPF	Y

5.4. V&V Reporting Task Analysis

All V&V activities related to the RPF Methodology were reported routinely and are documented within this report. Additionally, all published and presented research was submitted to the DTRA Public Affairs Office for review and release approval prior to publication and/or wider distribution.

6. V&V RECOMMENDATIONS

The penetration of both mono-energetic and poly-energetic neutron spectra into a steel cube, an armored cube, and a pair of nested steel cubes was investigated, along with commensurate free-field measurements. The penetration of multiple gamma ray spectra into an identical set of shielded enclosures was likewise investigated. In every neutron and gamma investigation, the experimental design was replicated in MCNP6 and a neutron and/or gamma spectra was computed. From these measurements and equivalent computations, NPF, GPF, and/or RPF values were determined both experimentally and computationally. Despite documented differences between

measured and computed spectra in all cases, these inequities resulted in <10% disparity between the measured and MCNP6-estimated RPF values.

Based upon the assembled data and research findings, the RPF Research Team recommends both DTRA and USANCA consider the RPF methodology and MCNP6 officially verified and validated to provide RPF estimates for vehicle surrogates at this time. These studies by no means exhaust the subject of neutron and gamma penetration of surrogate vehicles, but they do provide the justification for future investigations into MCNP6-derived RPF estimates for full-scale military vehicles.

Despite the accuracy and consistency of MCNP6-derived RPF estimates for surrogate vehicles, the simplified geometries and materials utilized in all recent prior research limit the extrapolation of any V&V conclusions. In short, the challenge in accrediting MCNP6 to provide RPF estimates for full-sized military vehicles remains both complex and lengthy; the process will require several independent studies to adequately assess MCNP6 RPF correctness across multiple vehicle types and both prompt and residual radiation environments.

As such, this report's final V&V recommendation was not exclusively reached from the demonstrated conclusiveness of the assembled studies. In addition to these findings, a clear and timely requirement exists for the US Army and wider DoD to initiate such T&E as necessary to fully V&V a computational mechanism for ascribing accurate RPF values to currently fielded military vehicles. The DTRA RPF Research Team feels confident that MCNP6 can provide that capability to the US Army and DoD.

7. KEY PARTICIPANTS

MAJ Andrew Decker
Primary Investigator (PI)
Nuclear Science and Engineering Research Center (NSERC)
Defense Threat Reduction Agency
West Point, NY
Email: andrew.w.decker.mil@mail.mil

MAJ Samuel Heider
Nuclear Science and Engineering Research Center (NSERC)
Defense Threat Reduction Agency
West Point, NY
(845) 938-0094
Email: samuel.heider.mil@mail.mil

Dr. John McClory
Air Force Institute of Technology
Wright-Patterson AFB, OH
(937) 255-3636 x7308
Email: john.mcclory@afit.edu

Dr. Stephen McHale
United States Naval Academy
Annapolis, MD
(410) 293-6495
mchale@usna.edu

Dr. Justin Clinton
Air Force Institute of Technology
Wright-Patterson AFB, OH
(937) 255-3636 x4586
Email: justin.clinton@afit.edu

Dr. Marshall Millett
United States Naval Academy
Annapolis, MD
(410) 293-6456
Email: millett@usna.edu

MAJ William Erwin
Air Force Research Laboratory
Wright-Patterson AFB, OH
Email: william.erwin.2@us.af.mil

MAJ David Matters
Defense Threat Reduction Agency
Fort Belvoir, VA
Email: david.a.matters.mil@mail.mil

8. REFERENCES

[1] C.J. Werner (editor), "MCNP Users Manual - Code Version 6.2", LA-UR-17-29981 (2017).

[2] R. Schwenk, A. Rainis and R. Rexroad, "Nuclear Vulnerability Analysis of the US M60A1 Tank in an Initial Radiation Environment (#1998)," US Army Armament Research and Development Command, Aberdeen Proving Grounds, 1977.

[3] C. R. Heimbach, "Final Report of Radiation Shielding in Armored Vehicles," Defense Technical Information Center, Alexandria, 1988.

[4] C. Eisenhauer and L. Spencer, "Approximate Procedure for Calculating Protection From Initial Nuclear Radiation From Weapons," National Bureau of Standards Center for Radiation Research, Gaithersburg, 1988.

[5] C. R. Heimach, "Radiation Protection-Factor Measurements of a Lined Iron Box in Simulated Fission and Fusion Tactical Nuclear Environments," Army Pulse Radiation Directorate, Aberdeen proving Grounds, MD, 1985.

[6] S. Stueker, A. E. Rainis and R. E. Rexroad, "Calculation of Residual Radiation Protection Afforded by the M113A1 Armored Personnel Carrier," US Army Armament Research and Development Command, Aberdeen Proving Grounds, 1978.

[7] S. Stueker, A. E. Rainis and R. M. Schwenk, "M113A1 Armored Personnel Carrier - Initial Radiation Protection Factors," US Army Armament Research and Development Command, Aberdeen Proving Grounds, 1978.

[8] H. Caton, "Radiation Transport Calculations of a Simple Structure Using the Vehicle Code System with 69-Group Cross Sections and the Monte-Carlo Neutron and Photon Code," Ballistic Research Laboratory, Aberdeen Proving Grounds, 1989.

[9] H. Caton and J. A. Morrissey, "Radiation Protection Factors of Selected Light Vehicles Against Residual Radiation," US Army Laboratory Command: Ballistic Research Laboratory, Aberdeen Proving Ground, 1988.

[10] S. Takahara et al., "Dose-reduction Effects of Vehicles against Gamma Radiation in the Case of a Nuclear Accident" January 2018, Health Physics 114(1):64-72, DOI: 10.1097/HP.0000000000000729)

[11] J. W. Durkee and M. R. James, "MCNP6 Verification and Validation for the MCNPX_65 and MCNPX_EXTENDED Test Sets," Los Alamos National Laboratory, Los Alamos, 2012.

[12] T. Goorley, M. James, T. Booth, F. Brown, J. Bull, L. J. Cox, J. Durkee, J. Elson, M. Fensin, R. A. Forster, J. Hendricks, H. G. Hughes, R. Johns, B. Kiedrowski, R. Martz, S. Mashnik, G. McKinney, D. Pelowitz, R. Prael, J. Sweezy, L. Waters, T. Wilcox & T. Zukaitis (2017) Initial MCNP6 Release Overview, Nuclear Technology, 180:3, 298-315, DOI: 10.13182/NT11-135

[13] K. G. Veinot and N. E. Hertel, "Effective Quality Factors for Neutrons Based on the Revised ICRP/ICRU Recommendations," *Radiation Protection Dosimetry*, vol. 115, no. 1-4, pp. 536-541, 2005.

[14] Reginatto, Paul Goldhagen, Sonja Neumann, "Spectrum unfolding, sensitivity analysis and propagation of uncertainties with the maximum entropy deconvolution code MAXED", Nuclear Instruments and Methods in Physics Research Section A: Accelerators, Spectrometers, Detectors and Associated Equipment, Volume 476, Issues 1–2, Pages 242-246, 2002

[15] M. Reginatto and P. Goldhagen, "MAXED, A Computer Code for the Deconvolusion of Multisphere Neutron Spectroscopy Data using the Maximum Entropy Method," Environmental Measurements Laboratory , New York, NY, 1998

[16] W. Erwin, "Verification and Validation of MCNP6 Using Gamma Protection Factor Measurements of an Iron Box," Air Force Institute of Technology, Dayton, 2015.

[17] A.W. Decker, M.P. Shannon, J.A. Clinton, J.W. McClory, S.R. McHale, "Verification and Validation of Monte Carlo N-particle Code 6 (MCNP6) with Neutron Protection Factor Measurements of an Iron Box", *Journal of Radiation Effects, Research and Engineering*, vol. 33, no. 1-E, pp. 252-259, May 2015.

[18] A. W. Decker, J. A. Clinton, J. W. McClory, M. Millett and S. R. McHale, "Verification and Validation of MCNP6.1 Neutron Protection Factor Estimates Using the WSMR FBR," *Journal of Radiation Effects, Research and Engineering,* vol. 35, no.1, pp. 52-58, 2016.

[19] J.D. Glesmann, M.G. Millett, M.E. Nelson, "Measurement and Model Validation of Neutron Protection Factors with a D-T Neutron Generator," Submitted to the Journal of Radiation Effects, Research and Engineering, vol. 35, 2017.

[20] T.J. Gates, C.R.Zeigler, C. Bouvier and A.W. Decker, "Verification and Validation of MCNP6.1 for Gamma Protection Factor Estimates of an Armored Box," *Journal of Radiation Effects, Research and Engineering,* vol. 35, no.1, pp. 83-90, 2016.

[21] J.L. Hall, S.J. Ha, R.D. Prins and A.W. Decker, ""Verification and Validation of MCNP6.1 Gamma Protection Factor Estimates Using an Armored Box and Phantom," *Journal of Radiation Effects, Research and Engineering,* vol. 35, no.1, pp. 103-110, 2016.

[22] A.W. Decker, S.A. Heider, S.R. McHale, J.A. Clinton, J.W. McClory, M. Millett, "Verification and Validation of MCNP6.1 Neutron Protection Factor Estimates of an Armored Vehicle Surrogate Using the WSMR Fast Burst Reactor," Journal of Radiation Effects, Research and Engineering, vol. 36, no.1, pp. 65-71, Apr. 2018.

[23] A.W. Decker, S.A. Heider, S.R. McHale, M. Millett, J.W. McClory, J.A. Clinton, "Validation of MCNP6 Neutron Spectra Estimates Using Nested Steel Cubes at the WSMR FBR," oral presentation delivered at the 2017 IEEE Nuclear Science Symposium and Medical Imaging Conference in Atlanta, GA on 26 October 2017.